Validation of Subject Specific Computed Tomography-based Finite Element Models of the Human Proximal Tibia using Full-field Experimental Displacement Measurements from Digital Volume Correlation

A Thesis Submitted to the

College of Graduate and Postdoctoral Studies

in Partial Fulfillment of the Requirements

for the Degree of Master of Science

in the Department of Mechanical Engineering

University of Saskatchewan

Saskatoon

By

Dylan Zaluski

PERMISSION TO USE

In presenting this thesis/dissertation in partial fulfillment of the requirements for a postgraduate degree from the University of Saskatchewan, I agree that the Libraries of this University may make it freely available for inspection. I further agree that permission for copying of this thesis/dissertation in any manner, in whole or in part, for scholarly purposes, may be granted by the professor or professors who supervised my thesis/dissertation work or, in their absence, by the Head of the Department or the Dean of the College in which my thesis work was done. It is understood that any copying or publication or use of this thesis/dissertation or parts thereof for financial gain shall not be allowed without my written permission. It is also understood that due recognition shall be given to me and to the University of Saskatchewan in any scholarly use which may be made of any material in my thesis/dissertation.

DISCLAIMER

Requests for permission to copy or to make other uses of materials in this thesis/dissertation in whole or part should be addressed to:

Head of the Department of Mechanical Engineering
57 Campus Drive
University of Saskatchewan
Saskatoon, Saskatchewan S7N 5A9 Canada

OR

Dean
College of Graduate and Postdoctoral Studies
University of Saskatchewan
116 Thorvaldson Building, 110 Science Place
Saskatoon, Saskatchewan S7N 5C9 Canada

ABSTRACT

Quantitative computed tomography-based finite element (QCT-FE) modeling is a computational tool for predicting bone's response to applied load, and is used by musculoskeletal researchers to better understand bone mechanics and their role in joint health. Decisions made at the modeling stage, such as the method for assigning material properties, can dictate model accuracy. Predictions of surface strains/stiffness from QCT-FE models of the proximal tibia have been validated against experiment, yet it is unclear whether these models accurately predict internal bone mechanics (displacement). Digital volume correlation (DVC) can measure internal bone displacements and has been used to validate FE models of bone; though, its use has been limited to small specimens.

The objectives of this study were to 1) establish a methodology for high-resolution peripheral QCT (HR-pQCT) scan acquisition and image processing resulting in low DVC displacement measurement error in long human bones, and 2) apply different density-modulus relationships and material models from the literature to QCT-FE models of the proximal tibia and identify those approaches which best predicted experimentally measured internal bone displacements and related external reaction forces, with highest explained variance and least error.

Using a modified protocol for HR-pQCT, DVC displacement errors for large scan volumes were less than 19μm (0.5 voxels). Specific trabecular and cortical models from the literature were identified which resulted in the most accurate QCT-FE predictions of internal displacements (RMSE%=3.9%, R^2>0.98) and reaction forces (RMSE%=12.2%, R^2=0.78). This study is the first study to quantify experimental displacements inside a long human bone using DVC. It is also the first study to assess the accuracy of QCT-FE predicted internal displacements in the tibia. Our results indicate that QCT-FE models of the tibia offer reasonably accurate predictions of internal bone displacements and reaction forces for use in studying bone mechanics and joint health.

PREFACE

Chapters 4 and 5 of this thesis have been drafted as (unsubmitted) co-authored manuscripts. I have provided contribution of the co-authors for both manuscripts-in-progress below.

Manuscript 1 – Chapter 4:

Zaluski, D., Kontulainen, S., Johnston, J.D. Precision of Internal Displacement Measurements in Long Bones Using HR-pQCT and Digital Volume Correlation. *Manuscript in preparation.*

Author's contributions: Dylan Zaluski contributed to study design, scan acquisition, image analysis, statistical analysis, data interpretation and drafted the manuscript. Dr. Saija Kontulainen provided supervision and was a key editor. Dr. JD Johnston contributed to study design, provided supervision, and was a key editor.

The results of this study were presented at an international conference:

i. Zaluski, D., Kontulainen, S., Johnston, J.D. Error of displacement measurements in long bones using digital volume correlation and high resolution peripheral quantitative computed tomography. Proceedings of the Canadian Society for Mechanical Engineering International Congress 2020, Charlottetown, PEI, June 2020.

Manuscript 2 – Chapter 5:

Zaluski, D., Kontulainen, S., Johnston, J.D. Experimental Validation of Finite Element Models of the Proximal Tibia for Internal Displacements and External Reaction Forces Using Digital Volume Correlation: The Effect of Assigned Material Properties. *Manuscript in preparation.*

Author's contributions: Dylan Zaluski contributed to study design, experimental testing and scanning, image analysis, finite element analysis, statistical analysis, data interpretation and drafted the manuscript. Dr. Saija Kontulainen provided supervision and was a key editor. Dr. JD Johnston contributed to study design, provided supervision, and was a key editor.

The results of this study were presented at an international conference:

i. Zaluski, D., Kontulainen, S., Johnston, J.D. Experimental validation of finite element models of the proximal tibia using digital volume correlation. The American Society for Bone and Mineral Research Annual Meeting 2020, Seattle, WA, September 2020.

ii. Zaluski, D., Kontulainen, S., Johnston, J.D. Error of displacement measurements in long bones using digital volume correlation and high resolution peripheral quantitative computed tomography. Proceedings of the Canadian Society for Mechanical Engineering International Congress 2020, Charlottetown, PEI, June 2020.

ACKNOWLEDGEMENTS

I would like to thank my supervisors, Dr. J.D. Johnston and Dr. Saija Kontulainen. You have taught me so much in these last two years, and I am grateful for your guidance and support.

Thank you to the members of our research group, your encouragement, advice, and shared experiences were extremely valuable. Having friends like you to work alongside made the struggles manageable.

Thank you to Rob Peace, our departmental assistant, you made many aspects of this project possible. It was a pleasure to work with you, and your dedication to helping others reach their goals is admirable and inspiring.

Thank you to my friends and family, I greatly appreciate your love and support, especially when it was not always easy. I could not have done this without all of you.

Finally, I would like to thank the University of Saskatchewan and the College of Mechanical Engineering for supporting me financially.

TABLE OF CONTENTS

LIST OF TABLES

LIST OF FIGURES

LIST OF TERMS, ABBREVIATIONS AND SYBMOLS

TERMS	DEFINITION
Anisotropic	Material exhibiting different mechanical properties in different directions
Anterior	Frontal plane of the body, facing forward
Apparent density	Bone specimen mass divided by total specimen volume (g/cm^3)
Ash density	Bone specimen ash mass divided by total specimen volume (g/cm^3)
Axial	Oriented along longitudinal axis of body
Bone mineral density	Mass of bone mineral in specimen divided by total specimen volume
Bone volume fraction	Volume of mineralized bone per unit volume (BV/TV)
Cortical bone	Dense, compact bone tissue forming outer surface of skeleton
Distal	Situated further from the center of the body
E-BMD	Density-modulus relationship
Embalmed	Specimens preserved from decay by fixing in formalin
Fabric	Second rank tensor quantifying porous material anisotropy
In vivo	Experiment inside a living organism
Inferior	Situated towards the lower part of the body
Isotropic (material)	Material with similar properties in each direction
Isotropic (voxel)	Voxel with same dimensions in all directions
Lateral	Situated nearer the outside of the body
Medial	Situated nearer the middle of the body
Modulus	Measure of material’s resistance to deformation

Orthotropic	Anisotropic material with three mutually perpendicular planes of symmetry
Partial volume effect	Artifact that reduces density of voxel, due to inclusion of boundaries between tissues with large density differences
Poisson’s ratio	Ratio of transverse to longitudinal strain
Posterior	Rear plane of the body, facing backwards
Proximal	Situated closer to the center of the body
Radiolucent	Transparent to X-rays, compatible with computed tomography
Sagittal	Plane dividing body down the middle, into left and right portions
Subchondral bone	Bone underlying articular cartilage
Superior	Situated towards the upper part of the body
Trabecular bone	Spongy, cellular bone tissue, comprised of rods and plates
Transverse	Plane dividing body into superior and inferior sections
Voxel	Volume element in three-dimensional space, 3D pixel

ABBREVIATIONS	DEFINITION
µCT	Micro computed tomography
µCT-DVC	Micro computed tomography-based digital volume correlation
µFE	Micro computed tomography-based finite element
2D	Two dimensional
3D	Three dimensional
BC	Boundary condition
BMD	Bone mineral density
BVF	Bone volume fraction
CT	Computed tomography
DCL	Digital command language
DIC	Digital image correlation
DOF	Degree of freedom
DVC	Digital volume correlation
DVC-FE	Finite element model validation using experimental measurements (strains/displacements) from digital volume correlation
E	Elastic modulus
EBE	Element-by-element
E-BMD	Density-modulus
FE	Finite element
FFT	Fast Fourier transform
FWHMH	Full width at half maximum height
GST	Gray-level structure tensor

HA	Hydroxyapatite
HR-pQCT	High resolution peripheral quantitative computed tomography
HU	Hounsfield units
K_2HPO_4	Dipotassium phosphate
LOOCV	Leave-one-out cross-validation
LSC	Least significant change
NLM	Non-local means
OA	Osteoarthritis
PCG	Preconditioned conjugate gradients
PSF	Point spread function
PV	Partial volume
QCT	Quantitative computed tomography
QCT-FE	Quantitative compute tomography-based finite element
RMSE	Root-mean-square error
RMSE%	Root-mean-square error percentage
SD	Standard deviation
SD_{rms}	Root-mean-square standard deviation
SNR	Signal-to-noise ratio
SR-µCT	Synchrotron micro computed tomography
TKR	Total knee replacement
TVD	Total variation denoising
VOI	Volume of interest

SYMBOLS	DEFINITION
ρ	Density
σ	Stress
ε	Strain
λ	Fabric eigenvalue
Π	Second invariant of the fabric tensor
µ	Micro
D	Material stiffness matrix
E	Elastic modulus
F	Finite element reaction force vector
G	Giga (e.g., GPa = Gigapascal)
g	Gradient in image intensity
K	Finite element stiffness matrix
kV	Kilovolt
M	Mega (e.g., MPa = Megapascal)
mA	Milliamp
mm	Millimeter
ms	Millisecond
N	Newton
Pa	Pascal (N/mm^2)
q	Finite element nodal displacement vector
R^2	Linear regression coefficient of determination
RF	Reaction force

CHAPTER 1

1 INTRODUCTION

1.1 Overview

Finite element (FE) modeling has become a valuable tool in the field of musculoskeletal research, allowing for non-invasive, *in-vivo* estimation of mechanical behaviour in human bones and soft tissue. Subject-specific bone geometry and material properties can be incorporated using quantitative computed tomography (QCT) to account for variations in an individuals' bone structure [1]. These models, referred to as QCT-FE, have applications in the research of osteoarthritis (OA), a whole-joint disease [2,3] affecting both cartilage and bone, with 1 in 8 Canadians affected [4]. QCT-FE models of the proximal tibia have been used to study the effects of altered bone mechanics on stress distributions in bone [5,6] and the overlying articular cartilage [7] in efforts to better understand the role of bone in OA initiation and progression. Other applications of QCT-FE include assessing bone strength of individuals with increased fracture risk [8,9] and optimization of total joint replacement implant designs [10–12]. Before these models gain more widespread adoption, it is important that their accuracy first be thoroughly validated.

As part of the QCT-FE modeling process, imaged bone mineral density (BMD) is used to estimate local mechanical properties using mathematical relationships (density-modulus, or E-BMD) from the literature [13]. Due to variations in the loading conditions experienced throughout the body, E-BMD relationships vary depending on anatomical site [14]. Furthermore, differences in testing methodology (ultrasonic vs. mechanical testing, specimen shape and size, etc.) have resulted in numerous proposed relationships, even for the same anatomical location. The choice of E-BMD relationship(s) can dictate model accuracy [15–17]. Therefore, guidance is necessary to select the optimal relationships for a given situation. Previous studies have identified the trabecular and cortical-specific E-BMD which result in the most accurate QCT-FE predictions of local subchondral stiffness for the proximal tibia [18,19]. It is unclear, however, if such models are also valid for internal bone displacement.

An emerging image processing technique known as digital volume correlation (DVC) is capable of measuring internal, 3D bone displacements with high-accuracy using micro-CT (μCT) [20]. DVC has been used to validate FE predictions of internal bone displacements [21–23], but analysis has been limited to relatively small volumes. High resolution peripheral QCT (HR-pQCT) is a clinical medical imaging tool designed with an open-ended, wide bore that can accommodate large specimens and directly image the micro-architectural details of trabecular bone, which is vital for DVC studies. Being a clinical tool, HR-pQCT is also more readily available than larger, custom μCT or synchrotron CT systems. The use of HR-pQCT with DVC has been limited [24,25], however, and artifacts specific to its large volume scanning techniques have not been addressed.

The overall aim of my thesis was to validate QCT-FE modeling approaches for the human proximal tibia for both global reaction forces and internal bone displacements. The first objective was to develop a methodology for measuring experimental internal bone displacements in long human bones using HR-pQCT imaging and DVC. The second objective was to create QCT-FE models of the proximal tibia using different trabecular/cortical density-modulus relationships from the literature and identify those which best predicted experimentally measured internal bone displacements and external reaction forces, with highest explained variance and least error.

1.2 Scope

Chapter 2 provides a review of the relevant literature, focusing on knee joint anatomy, bone structure, joint health, the FE modeling technique and its application to human bone, and the validation of QCT-FE models through traditional techniques as well as DVC. Chapter 3 outlines research questions and defines the objectives of this work. In Chapter 4, the precision errors associated with internal displacement measurements in long bones using DVC with HR-pQCT imaging are reported. In Chapter 5, QCT-FE models of the proximal tibia are validated against experimental internal displacements and external reaction forces using the HR-pQCT and DVC protocol outlined in Chapter 4. Chapter 6 provides an overview of the findings, discusses the research contributions from this thesis and the clinical significance, and provides suggestions for future research.

CHAPTER 2

2 LITERATURE REVIEW

2.1 Functional Anatomy

2.1.1 Knee joint

The knee is a complex lower-limb joint tasked with supporting bodyweight during standing and locomotion while also permitting a high degree of flexibility. Three bones comprise the joint: the femur, tibia, and patella (see Figure 2-1, patella not shown). Articulation occurs between the femur and tibia, forming the tibiofemoral joint, as well as between the patella and the femur, forming the patellofemoral joint. (The proximal tibia has been the subject of several computer modeling studies investigating bone stress and stiffness and their relation to OA [5,6,26], and will be the focus of this study). Joint stability is provided by ligaments which connect the bones, minimizing the risk of dislocation [27]. Smooth articulation between the femur and tibia is facilitated by the articular cartilage (covering the femoral condyles and tibial plateaus), a complex poro-viscoelastic tissue with high compressive stiffness and excellent load distribution capabilities [28]. The menisci (two crescent-shaped wedges of fibrous cartilage attached to the medial and lateral tibial plateaus, overlying the articular cartilage) further facilitate load distribution [27]. Besides soft tissue, bone structure also plays an important role in the transfer of load through the tibiofemoral joint. Relevant to this study, mechanical stress in articular cartilage has been shown to be dependent on the stiffness properties of underlying bone [7,29,30].

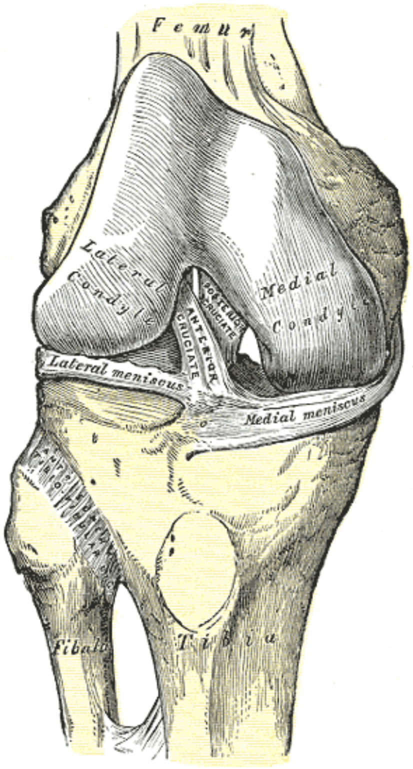

Figure 2-1 Anterior view of the knee joint, with the patella removed, showing the distal femur, proximal tibia and proximal fibula, as well as the surrounding soft and connective tissue. Modified from Gray’s Anatomy [31].

2.1.2 Types of bone

At a macro scale, long bones consist of two primary types of bone material: cortical (compact) and trabecular (cancellous) bone (Figure 2-2). Cortical bone is a dense, compacted tissue and constitutes the walls of the shafts (diaphyses) of long bones; within these walls is the medullary cavity, containing bone marrow [27]. Trabecular bone is located at the end-sites (epiphyses) of long bones and is comprised of a geometrically complex network of rods and plates. Due to its structural heterogeneity, trabecular bone exhibits a large degree of anisotropy, with different mechanical properties in different coordinate directions [32].

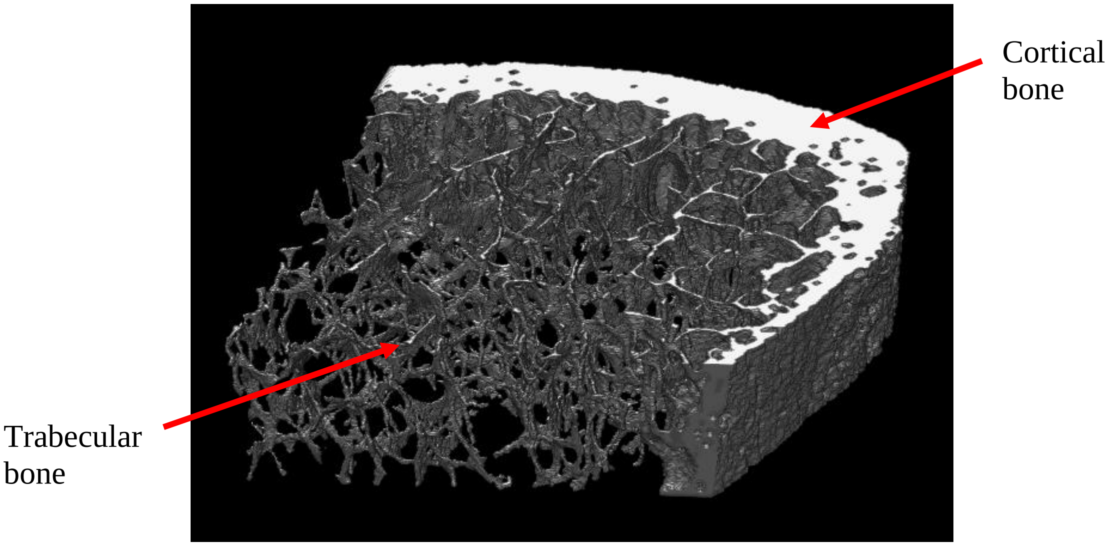

Figure 2-2 Volumetric rendering of a section of bone from the shaft of the proximal tibia, acquired by HR-pQCT, showing the geometrically complex trabecular bone surrounded by a dense cortex

2.1.3 Bony structure of the tibia

Seen in Figure 2-3, the tibia is comprised of several types of bone optimally arranged to support physiological loads encountered day-to-day. Along its shaft, the relatively uniform cortical bone is adapted to axial and bending loads produced during weight-bearing, gait, and elevated activity. Towards the proximal end of the tibia, trabecular bone becomes the primary component, and supports the majority of applied compressive load [33]. At the very proximal surface of the tibia, two compartments exist, forming the medial and lateral plateaus. The tibial compartments underlie the femoral condyles and are covered by the articular cartilage. Each compartment is made up of subchondral bone, which is itself comprised of several layers. Subchondral cortical bone is found directly beneath the articular cartilage and covers a layer of subchondral trabecular bone. An important function of the subchondral bone is to distribute impulsive loads, protecting the overlying articular cartilage [34].

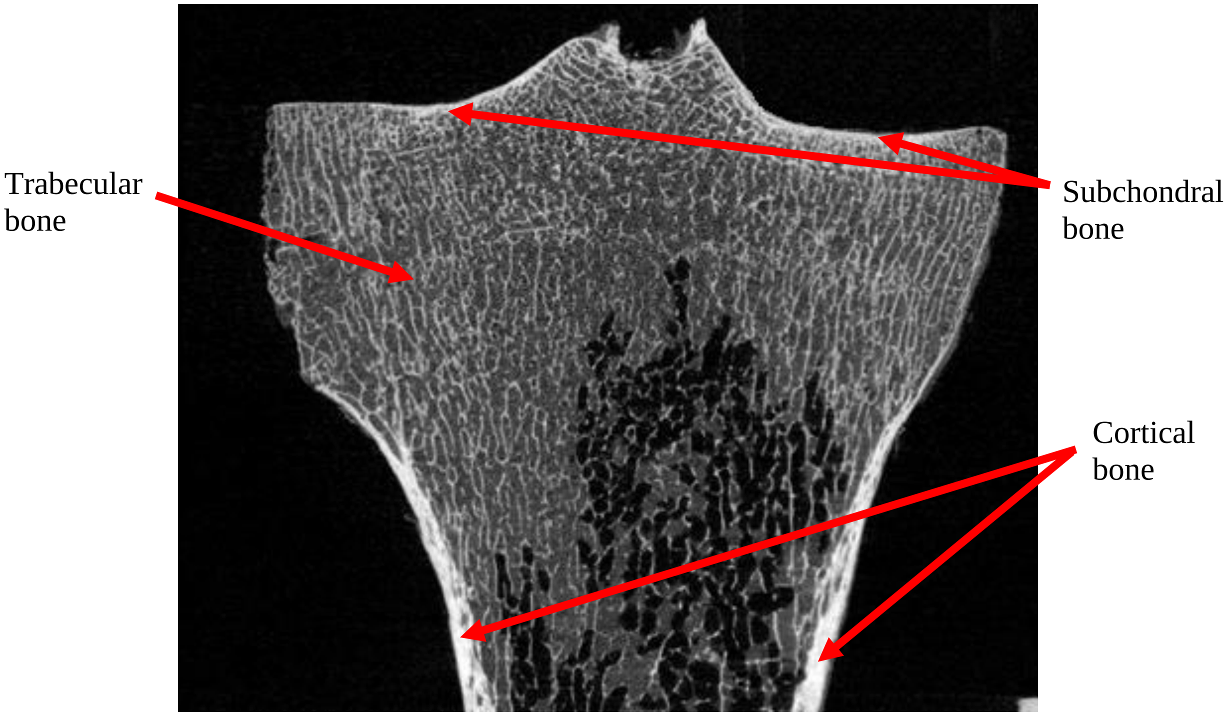

Figure 2-3 Cross section of a HR-pQCT scan of the tibia, showing its varying bone structure. Cortical bone forms the tibia shaft, and encapsulates the spongy trabecular bone. At the proximal surface, denser subchondral bone underlies the cartilage

2.2 Osteoarthritis and joint health

Osteoarthritis is a progressive joint disease which afflicts 1 in 8 Canadians [4], causing severe joint pain, stiffness, and disability. OA joints undergo morphological alterations including cartilage thinning, thickening of the subchondral plate, and the formation of cysts (essentially voids in subchondral bone) and osteophytes (bone spurs along peripheral edge of joint) [3] (Figure 2-4). Mechanically, OA bone exhibits an altered tissue modulus/stiffness [35–37] due to microstructural changes, including bone volume fraction (BVF) [36,37] and degree of anisotropy. The articular cartilage also experiences mechanical changes, with an altered effective elastic modulus and stiffness [35,38,39]. Although several theories have been proposed, the relationship between altered bone and soft tissue of OA joints is not yet fully understood.

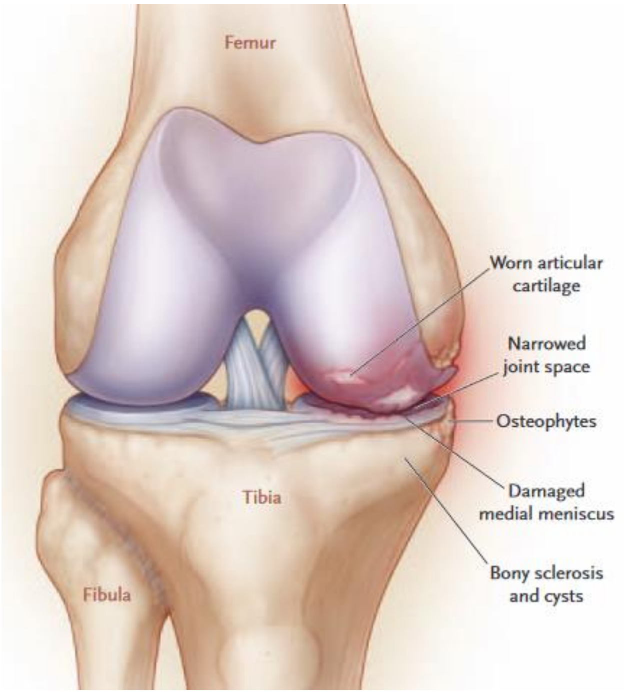

Figure 2-4 Example of an osteoarthritic knee joint, showing cartilage wear, meniscal damage, joint space narrowing and osteophyte formation. Reproduced with permission from Felson, 2006 [40], Copyright Massachusetts Medical Society.

In severe cases of knee OA, total knee replacement (TKR) may be required to restore joint function and alleviate pain. Fixation of TKR implants is not a trivial task and understanding how the implant interacts with the surrounding bone tissue is important. Stress-shielding occurs when the stiff implant stem carries load originally carried by the bone, reducing stresses in the surrounding bone [41–43]. According to Wolff's law [44], bone adapts to its mechanical environment; in the absence of adequate loading, bone resorption occurs, removing valuable bone material and potentially resulting in implant loosening or bone fracture from reductions in overall strength. Therefore, the choice of stem material and geometry is of particular concern.

While experimental and observational studies are extremely valuable for investigating OA and its treatments, there is information they cannot provide, such as stress and displacement distributions within a person's bone *in-vivo*, and the effects of geometrical and mechanical property alterations. Modern medical imaging methods, such as quantitative computed tomography (QCT), permit numerical studies for simulating controlled experiments without the need for expensive cadaver specimens or labor-intensive mechanical testing. These models have been used to differentiate between normal and OA knees [6], investigate potential factors of disease initiation/ progression [5,45–47], and examine the effect of implant material selection and geometry on post-TKR stress-shielding [10–12].

2.3 Finite Element Modeling

2.3.1 Overview

The finite element method is a computational analysis tool frequently used in engineering, with applications in structural analysis, acoustics and vibrations, fluid mechanics and heat transfer. By discretizing a complex domain into many smaller elements, geometrically and materially advanced problems can be solved that would be impossible analytically. In the context of static structural analysis, each finite element produces an element stiffness matrix, relating applied external loads to nodal displacements as a function of element geometry and material properties. Using information relating the connectivity between these different elements, a larger *global* stiffness matrix can be assembled, and a linear system of equations describing the entire system is obtained:

$$[\sum K_e]\vec{q} = \vec{F}, \tag{2-1}$$

where $\vec{q}$ is the nodal displacement vector and $\vec{F}$ is the global reaction force vector. The resulting system of equations can be massive (matrices consisting of millions of columns/ rows) and solving for the displacement field (and ultimately, stresses and strains) requires careful treatment.

2.3.2 Solution approaches

2.3.2.1 Direct

The direct solution of equation 2-1 requires first completing the assembly process, summing the local element stiffness matrices according to their row and column contributions in the global matrix. The assembled global stiffness matrix is often extremely sparse, with a small percentage of entries being non-zero. Selecting a suitable sparse matrix solver is critical to avoiding memory errors and extremely long computation times. The most well-known approach for direct solution of FE type problems is the Cholesky Decomposition, a variant of Gaussian Elimination which seeks a lower-triangular matrix L which when multiplied by its transpose recreates the original stiffness matrix, K [48]. It is important to note that the Cholesky Decomposition requires a symmetric, positive-definite (only positive eigenvalues) matrix, which is guaranteed in structural FE problems. After obtaining L, the degrees of freedom (DOF) vector $\vec{q}$ can be calculated by simple back-substitution. Modern direct FE solvers typically utilize a variant of the Frontal solution method, a memory-efficient version of Cholesky Decomposition that eliminates degrees of freedom when they are no longer required, saving factorizations to the hard drive for back-substitution later [49]. Multifrontal methods also exist for modern multi-core workstations [50].

2.3.2.2 Element-by-element

When solving FE models consisting of millions of DOFs (common for models derived from voxel data), it is undesirable to assemble the entire global stiffness matrix. Avoiding the assembly process altogether drastically reduces storage requirements, allowing for larger models to be run on lower-end hardware. When each element of an FE model is of the same type and shape, only one element stiffness matrix needs to be stored, which can then be scaled by different elastic moduli. Computing the matrix-vector product in equation 2-1 is simple and can be done on an element-by-element (EBE) basis, summing terms based on their contributions to the DOFs while never assembling the full stiffness matrix. Iterative solvers like the method of preconditioned conjugate gradients (PCG) turn a memory-intensive task into a computationally intensive one. Instead of factorizing the entire system, a large number of simple, easily parallelizable matrix-vector products are performed [51] (Figure 2-5). Like all iterative methods, PCG starts with an initial guess for the solution vector, and loops through the main algorithm body until the objective function is smaller than a specified convergence tolerance; often, the norm of the residual vector, r_0, is used. In PCG, a preconditioner M is used to accelerate convergence. This preconditioner must be computationally cheap to construct and easily invertible. Using the diagonal of the global stiffness matrix, also known as Jacobi preconditioning, is commonplace in EBE FE solvers [52,53]. The diagonal is inexpensive to construct and store, and inversion is a simple matter of taking the reciprocal of each term. Huge memory savings and quick convergence make the PCG-based EBE solution method ideal for very large models, typical of voxelized CT scans.

```
Input: $A$ – symmetric, positive-definite matrix; $b$ – right hand side; $x_0$ – initial solution guess
Output: $x$ – solution vector
$r_0 = b - Ax_0$
$z_0 = M^{-1} r_0$
$p_0 = z_0$
For $k = 0, 1, 2, \ldots$
    $\alpha_k = \frac{r_k^T z_k}{p_k^T A p_k}$
    $x_{k+1} = x_k + \alpha_k p_k$
    $r_{k+1} = r_k - \alpha_k A p_k$
    If $r_{k+1} \cong 0$ then exit loop
    Else
        $z_{k+1} = M^{-1} r_{k+1}$
        $\beta_k = \frac{r_{k+1}^T z_{k+1}}{r_k^T z_k}$
        $p_{k+1} = z_{k+1} + \beta_k p_k$
    End if
End for
```

Figure 2-5 General algorithm for solving $Ax=b$ using the method of preconditioned conjugate gradients, an iterative Krylov subspace method [54]

2.3.3 Modeling approaches for bones

Two paradigms exist for FE modeling of human bones and joints: generic modeling, and subject-specific modeling. Generic FE models incorporate idealized geometry and material properties representative of a typical bone [26,55] (Figure 2-6), and are useful for parametric studies investigating the effects of changing model properties to represent different populations or disease states, or optimizing bone implant geometry [11]. For bones like the tibia, simplifying the model as axisymmetric can decrease computational cost substantially.

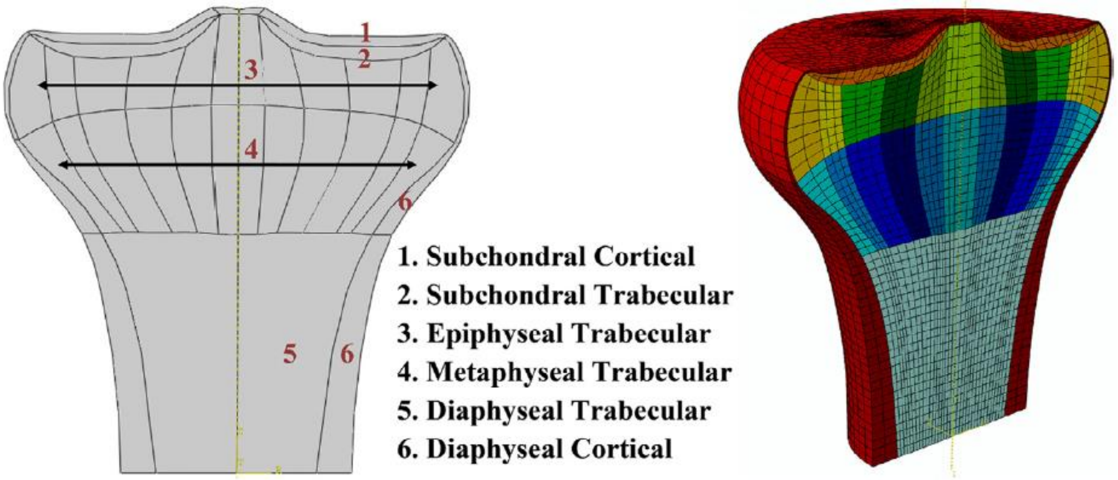

Figure 2-6 Axisymmetric FE model of the human proximal tibia incorporating generalized bone geometry and material properties. Modified from Amini et al. [26]

Subject-specific FE models, although much more complex, produce more accurate predictions of mechanical behaviour than generic models and have become the standard approach to human modeling. Subject-specific models have been used to assess fracture risk [8,9,17] and predict implant stability for joint replacements [56]. Bone geometry is acquired via a non-invasive 3D medical imaging modality. Typically, clinical QCT is used, as it is readily available and can quantify variations in internal bone structure/density. A variety of techniques exist for manually, semi-automatically or automatically extracting the bone surface from the surrounding tissue in the volumetric images and make up an entire field of image processing known as image segmentation. From the voxelized segmentations, a FE mesh must be produced that well approximates the bone geometry.

2.3.3.1 Voxel-based meshing

The simplest meshing approach involves converting each QCT voxel labelled as bone during segmentation into a linear hexahedral finite element (Figure 2-7a). This voxel-based meshing approach is the method of choice for micro-FE models incorporating bone micro-architecture [53,57] and has been used for clinical QCT-based FE modeling as well [8,58,59]. The method is attractive due to several strengths: the direct conversion of voxel to element without geometry-smoothing facilitates automatic model generation; element deletion does not require a complete remeshing; and using a single element type/geometry avoids inaccuracy caused by element distortion and facilitates the use of an EBE solver for memory efficiency. However, there are some drawbacks to the geometrical inaccuracies of voxel-based meshes. Specifically, to achieve reasonable accuracy, a relatively high-resolution mesh is required, resulting in models of hundreds of thousands or millions of elements [60]. Larger voxel sizes (greater than 1mm) do not well represent the bone surface, and thus exhibit convergence issues [59] due to erroneous stress concentrations caused by the jagged boundary.

2.3.3.2 Geometry-based meshing

Another approach to meshing QCT-FE models is the geometry-based method, which attempts to best approximate the smooth bone surface using elements of varying sizes, shapes and aspect ratios (Figure 2-7b). After image segmentation, the bone geometry is first approximated by converting the voxelized volume into a triangulated surface mesh (stereolithography file) by the marching cubes algorithm [61]. To remove small peaks and valleys present in the triangulated model, non-rational uniform B-splines (NURBS) are commonly used to represent the final surface, retaining important geometrical features [6,15]. Using hexahedral or tetrahedral finite elements, a mesh is generated to represent the bone geometry. Although hexahedral elements have been found to produce more accurate model predictions [60], quadratic tetrahedral elements are more commonly used [15,62,63] due to the robustness of automatic tetrahedral meshing.

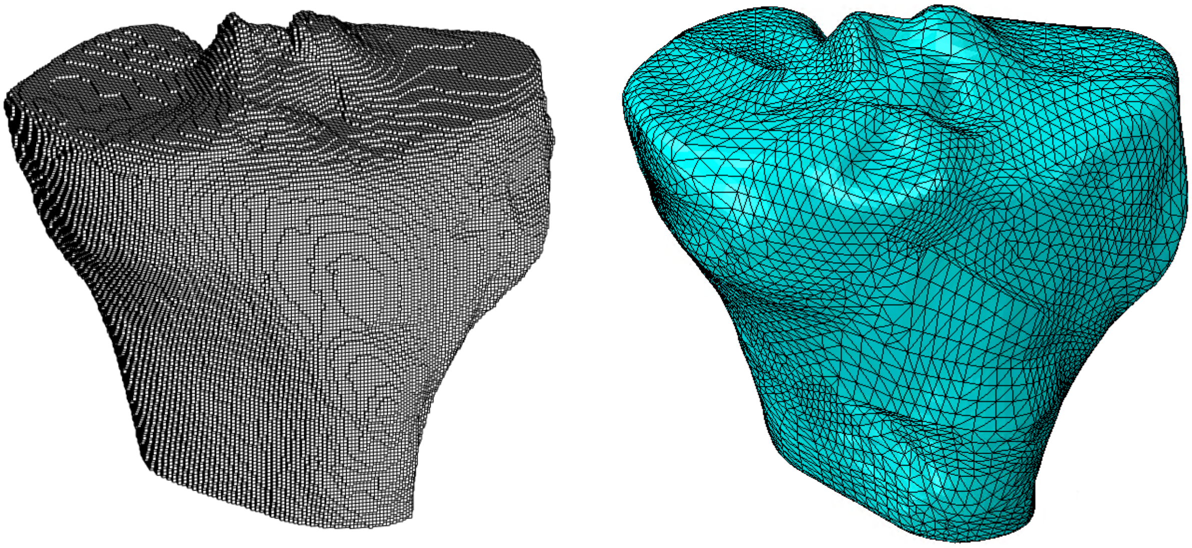

(a) (b)

Figure 2-7 Subject-specific FE models generated from QCT data, derived using a (a) voxel-based mesh with hexahedral elements, and (b) a geometry-based mesh with tetrahedral elements

Using a geometry-based QCT-FE model has several advantages: surface stress/strain predictions are more trustworthy; and element counts are generally much lower when compared to voxel-based meshes, reducing computation time. Yet, geometry-based models have not altogether replaced voxel-based models, due to some inherent disadvantages. Accurately representing the bone surface with triangulation and NURBS fitting takes more computational effort and is less robust (i.e., harder to automate). The range of element shapes and sizes requires that care be taken to avoid distorted elements, which would affect model accuracy [64]. Assigning material properties to each element is also non-trivial when they do not conform to the QCT grid system.

2.3.4 Density-modulus relationships

When the fine micro-architectural details of trabecular bone can be directly modeled, as is the case for µCT-based FE (µFE), bone's mechanical properties are often generally considered to be isotropic (identical in all directions) and independent of density [32], and a single value for elastic modulus is used throughout the whole model [52,57]. For QCT-FE models where each element may contain many trabeculae, the assumption of uniform material properties no longer holds, and the spatial distribution of material properties must be accounted for. Using rods of known concentrations of hydroxyapatite (HA) or hydrogen dipotassium phosphate (K_2HPO_4), a calibration equation can be measured to convert CT Hounsfield units (HU) to local BMD [65]. Measures of bone density (wet/dry, apparent, ash, etc.) can then be used to estimate an effective elastic modulus (E) using empirical density-modulus (E-BMD) relationships from the literature [13] (Figure 2-8). To obtain these E-BMD relationships, mechanical [14,66,67] or ultrasonic [68–70] testing is performed to measure the effective elastic modulus of excised bone samples. Regression is used to fit a relationship between measured sample density and effective modulus, usually in the form of a power-law. Variations in sample pool (anatomical site, bone type), sample geometry (cylinder or cube), and mechanical testing end conditions (platen or end-cap) have resulted in a wide range of predicted E for a given density [32], making the choice of E-BMD equation for a particular modeling study a complex one. Of the many published E-BMD relationships for human bone, some are derived solely from excised trabecular samples from human tibiae [14,69,71], while others pool tibia samples with other samples from other anatomical locations [14,66]. To complicate things further, BMD alone cannot explain all variations in the mechanical properties of bone [72]. Specifically, trabecular bone's microarchitecture results in an inherently anisotropic material, which responds differently depending on the axis of load application.

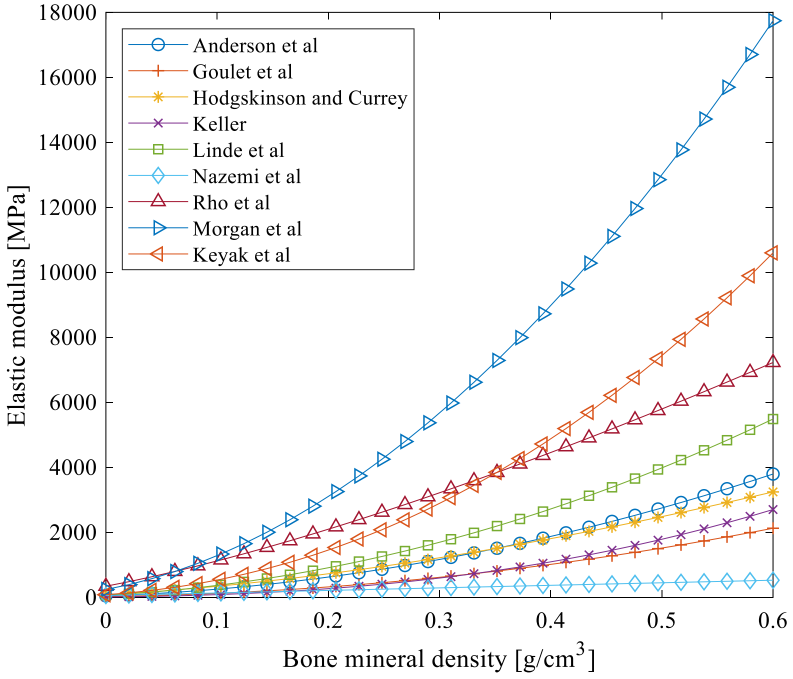

Figure 2-8 Trabecular bone density-modulus relationships from literature for different anatomical sites, including proximal tibia-specific and pooled datasets

2.3.5 Material orthotropy

As stated above, bone is often modelled as an isotropic material, with its mechanical behaviour exhibiting no directional dependencies. The resulting models are simple to create and yield accurate results when predicting the overall structural response but may not accurately represent internal mechanical behaviour [73]. As well as being strongly dependent on structural density, trabecular bone's mechanical behaviour also depends on its textural anisotropy [74], making it inherently orthotropic (direction-dependent material properties aligned with three mutually orthogonal planes of symmetry). Cortical bone also exhibits orthotropic behavior, but to a lesser extent [70] due to its lamellar structure and the orientation of collagen fibers.

In continuum mechanics, stress and strain are related by the material stiffness matrix, D, using the following equation:

$$\sigma = D\varepsilon, \tag{2-2}$$

where D is a 6 by 6 matrix. For definition, isotropic materials require one scalar value for the elastic modulus and one for Poisson's ratio. Orthotropic materials, on the other hand, require three unique values for the elastic moduli (one for each of the three coordinate axes), three for the shear moduli, and three for the Poisson's ratios. To reduce complexity, several studies have adopted the approach of assuming a uniform material orientation and anisotropy throughout the entire bone [8,63]. The antero-posterior and medial-lateral elastic moduli, as well as all 3 shear moduli, are calculated as simple ratios of elastic modulus along the long axis, as per experimental observations [70]. At the cortical shaft, anisotropy ratios remain fairly constant [68]. However, towards the proximal end of the tibia, the degree of anisotropy of the trabecular bone, and its orientation, are far more variable and simple ratios may not be appropriate.

Until recently, measuring trabecular bone anisotropy required high-resolution, µCT scans which are typically not attainable *in-vivo*. An emerging approach, using the gray-level structure tensor (GST), allows for measurement of trabecular bone anisotropy directly from clinical-resolution CT scans [75,76]. First, the intensity gradients (g_1, g_2, g_3) in three orthogonal directions are calculated at each voxel in the CT volume using a centered finite difference stencil. Sobel filters have also been used to calculate the local intensity gradients, but offer no benefit with large CT voxels [75]. For a cubic volume of interest (VOI), the GST is calculated as

$$K_{ij}=\sum_{m=1}^{r}\sum_{n=1}^{r}\sum_{l=1}^{r} g_i(m,n,l)\times g_j(m,n,l), \qquad 2\text{-}3$$

where r is the VOI width in voxels [76]. A normalized fabric tensor $\widehat{H}$ can then be formed as

$$\widehat{H}=3K^{-1/2}/trace(K^{-1/2}), \qquad 2\text{-}4$$

whose eigenvalues (λ_1, λ_2, λ_3) and eigenvectors represent trabecular anisotropy and orientation [75]. Using the fabric eigenvalues and Cowin's fabric-elasticity equations [77], the nine unique entries of the material stiffness matrix can be calculated for a local VOI:

$$D_{ii} = E_t(k_1 + 2k_6 + (k_2 + 2k_7)\Pi + 2(k_3 + 2k_8)\lambda_i + (2k_4 + k_5 + 4k_9)\lambda_i^2) \text{ for } i = 1, 2, 3$$

$$D_{ij} = E_t(k_1 + k_2\Pi + k_3(\lambda_i + \lambda_j) + k_4(\lambda_i^2 + \lambda_j^2) + k_5\lambda_i\lambda_j) \text{ for } i, j = 2 \text{ and } 3,\ i \neq j$$

$$D_{44} = E_t(k_6 + k_7\Pi + k_8(\lambda_2 + \lambda_3) + k_9(\lambda_2^2 + \lambda_3^2)) \qquad 2\text{-}5$$

$$D_{55} = E_t(k_6 + k_7\Pi + k_8(\lambda_1 + \lambda_3) + k_9(\lambda_1^2 + \lambda_3^2))$$

$$D_{66} = E_t(k_6 + k_7\Pi + k_8(\lambda_1 + \lambda_2) + k_9(\lambda_1^2 + \lambda_2^2))$$

where: $k_m = k_{am} + k_{bm}\rho^p$, ρ is BMD, k are 18 empirically determined coefficients, p is an empirically determined exponent, E_t is the assumed bone tissue elastic modulus, and $\Pi = \lambda_1\lambda_2 + \lambda_1\lambda_3 + \lambda_2\lambda_3$. With samples of trabecular bone from the distal radius, Nazemi et al. derived the 19 coefficients of the Cowin fabric-elasticity equations for use with clinical QCT images, explaining 97% of the variance in material stiffness entries when compared to gold-standard micro-FE [76]. For QCT-FE models, these coefficients along with equation 2-5 can be used to incorporate spatially varying anisotropy, with a unique material stiffness matrix for every element [78].

2.3.6 Material mapping

Material properties obtained from QCT must be mapped to the individual elements. In the case of voxel-based meshes, each element corresponds directly to a QCT voxel, making the mapping process trivial: elements are simply assigned material stiffness matrices determined by the E-BMD relationships or fabric-elasticity equations described in sections 2.3.4 and 2.3.5. (Figure 2-9). The material mapping procedure becomes more complicated when a geometry-based FE model is used. Numerous methods have been proposed in the literature: averaging the properties of all voxels contained with an element [1,18]; numerically integrating the property field over the element [79]; assigning properties at element nodes [62,80]; or assigning properties at each element integration point [80,81]. Depending on the FE software package, there may also be limitations for the number of unique materials permitted, requiring a binning process to group similar properties [1,79].

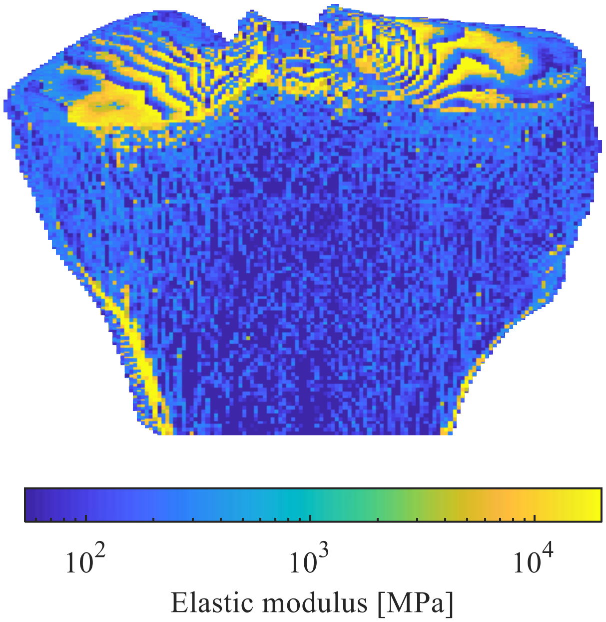

Figure 2-9 Voxel-based QCT-FE model with anterior side cut away, showing distribution of elastic moduli calculated from E-BMD and mapped to individual elements.

2.3.7 Experimental validation of QCT-FE models

Model accuracy is influenced by many factors, including the choice of meshing method [60], element size [59], E-BMD relationship(s) [18,82,83] and material mapping strategy [15,62]. Therefore, experimental validation is crucial before clinical application of any FE modeling methodology. To date, several studies have compared predictions from QCT-FE models of the tibia to experimental measurements. Gray et al. found excellent agreement (R^2=0.96, RMSE%=9.0%) when comparing FE-predicted strains to experimental measurements from a single fresh-frozen human tibia instrumented with 17 strain gauge rosettes and subjected to macro-indentation, torsion and four-point bending [63]. There were, however, significant limitations to Gray's study: the results only reflected a single specimen, only one material mapping strategy and set of E-BMD relationships was tested, and measured strains were limited to the cortical surface, distant from the subchondral bone. Edwards et al. evaluated QCT-FE predictions of torsional stiffness and fracture, reporting error of less than 10% when compared to experimental testing data of 11 formalin-fixed cadaver specimens [8]. Both Gray and Edwards utilized the same trabecular E-BMD relationship [69] and incorporated orthotropic material properties using constant ratios relating the different elastic and shear moduli [70]. It is important to note that these orthotropic properties were based on measurements from cortical bone but were applied to the entire density range in both studies, despite the heterogeneous anisotropy of trabecular bone.

For FE models intended for the study of knee OA or tibiofemoral joint repair, the accuracy of predictions in the proximal tibia near the subchondral surface are of primary concern. Recently, a set of studies comparing FE-predicted subchondral bone stiffness to experimental stiffness investigated the effects of different E-BMD relationships [18,19] and material models [78] on QCT-FE accuracy. Thirteen proximal tibia compartments were imaged and subjected to macro-indentation stiffness testing. The choice of E-BMD relationship(s) from literature resulted in models with varying accuracy (RMSE% from 16.6% to 337.6%) and predictive ability (R^2 from 0.56 to 0.77), and the incorporation of spatially varying anisotropic trabecular bone properties resulted in further improvements to model accuracy (RMSE%=11.2%) [78]. Despite good agreement between FE and experiment for external measures of bone mechanical behaviour, it is unclear how well QCT-FE models predict internal bone displacements in the proximal tibia, and which choices of model parameters are most appropriate. The stems of TKR implants are fixated within the trabecular bone, and important clinical OA symptoms such as pain have been linked to elevated internal bone stresses [84]; therefore, it is important that internal bone mechanics be accurately characterized by FE.

2.4 Digital volume correlation

While strain gauges have been used for decades for studying bone mechanics due to their simplicity and accuracy, they have inherent limitations. Strain measurements are limited to surface measurement of cortical bone, and only at select, discrete points where gauges can be applied. Digital image correlation (DIC) is an optical method for measuring surface displacements over a much larger field and has been used in place of surface strain gauges for cortical bone [85–87]. Unlike strain gauges, DIC does not require a complicated cleaning and gluing process and can capture measurements at hundreds or thousands of sample points with ease. Neither strain gauges nor DIC, however, can measure the response of trabecular bone in its native environment, as it is obscured by the cortex. Digital volume correlation is a 3D extension of DIC, first introduced by Bay et al. in 1999 [20]. By comparing two high-resolution image volumes, one undeformed and the other deformed, DVC can track internal displacements non-invasively. Image acquisition is typically performed with µCT [88–93], although other modalities such as synchrotron µCT (SR-µCT) [94–96] and HR-pQCT [24,25] have also been used. Two fundamentally different approaches are adopted in the literature for tracking displacements: local and global DVC.

2.4.1 Local DVC

The first step of the local DVC approach is to select suitable sample points within the volume. The undeformed image volume is divided evenly into smaller non-overlapping volumes, called subvolumes, with the point at their center corresponding to the point of measurement. Next, the goal is to search the deformed image volume to find the new location of each subvolume from the undeformed image volume. Searching is done by shifting and deforming the subvolume until it best matches a local region of the deformed image. The accuracy of the match is measured by the normalized cross-correlation coefficient, which is defined for a shift *dx, dy, dz* as [97,98]:

$$C(dx,dy,dz) = \frac{\sum_{i,j,k}(A_{i,j,k} - \langle A\rangle)(B_{i+dx,j+dy,k+dz} - \langle B_{dx,dy,dz}\rangle)}{\sqrt{\sum_{i,j,k}(A_{i,j,k} - \langle A\rangle)^2}\sqrt{\sum_{i,j,k}(B_{i+dx,j+dy,k+dz} - \langle B_{dx,dy,dz}\rangle)^2}}, \qquad \text{2-6}$$

where i, j and k are the coordinates of the subvolume in the reference image, A is the reference image, B is the deformed image, and $\langle A\rangle$ and $\langle B_{dx,dy,dz}\rangle$ are the arithmetic means of the reference and deformed image subvolumes. For non-integer shifts, trilinear or tricubic image interpolation is employed. At each DVC sample point, the measured displacement is selected as the set of subvolume shifts and deformations that result in the largest normalized correlation coefficient (which ranges from 0 when there is no common information to 1 when the reference and deformed regions are a perfect match). Sophisticated local DVC software packages use a non-constant subvolume size. *DaVis DVC*, a commercial tool from *LaVision GmbH* [97], performs an initial integer search of the whole image space using the Fast Fourier transform (FFT) with a large subvolume size, followed by several iterative, sub-voxel refinements using successively smaller subvolumes. This approach allows DVC to capture large deformations reliably and quickly. Since the correlation process is entirely independent for each measurement point, the local approach is easily parallelizable. However, this locality does have a drawback: there is no enforcement of connectivity between DVC sample points, making it possible for displacements to be measured that are not physically realizable (measurement points crossing each other).

2.4.2 Global DVC

Similar to local correlation, a global approach also begins with a discretization of the measurement domain. Measurement points are marked as nodes, which are then connected to each other to form the measurement volume. Nodal connectivity is stored similar to the finite element approach for structural simulation. Calculating the nodal displacements involves enforcing optical flow conservation between the reference and deformed image volumes by minimizing an objective function [99,100]:

$$F = \iiint_D [g(x) - f(x + U(x))]^2 dx, \tag{2-7}$$

where $f(x)$ is the reference image volume, $g(x)$ is the deformed image volume, and $U(x)$ is a trial deformation field. Equation 2-7 must be linearized, and the deformation field term $U(x)$ is approximated using shape functions for linear 8-node hexahedral finite elements. Minimization is then reduced to the iterative solution of a linear system of equations. Much like local DVC, a multi-scale approach is commonly used to refine the displacement field [99]. Coarser steps are performed by filtering and downsampling (averaging) the image volumes to reduce computational costs, with the algorithm eventually performing the minimization on the full dataset for the final displacement field. The global DVC approach, while more robust due to enforced connectivity, is more computationally demanding since calculation of nodal displacements requires information about the whole system [101]. Accuracy may also be lower in the case of local specimen failure or fracture, as the nodal connectivity may no longer represent the physical arrangement of material. Regardless of the correlation approach chosen, it is important that the limitations of the measurement method be understood and considered during experimental design and the interpretation of results.

2.4.3 Measurement error of DVC

Quantifying DVC measurement error is not as straightforward a task as comparing measurements to closed-form solutions for simple mechanical problems. Complications such as mechanical testing end-artifacts and material imperfections make the resulting internal displacement fields heterogeneous and complex. With no clear gold-standard to compare internal measurements to, there are two approaches commonly adopted in the literature for assessing DVC measurement accuracy: zero-strain testing and artificial shifting and straining. Zero-strain tests involve taking consecutive 3D scans of the same sample with no loading or repositioning, and then measuring the associated displacement fields using DVC [20,98]. Displacement accuracy is regarded as the mean measured displacement in the zero-strain test, and the displacement precision is regarded as the standard deviation (SD) of the displacement fields. Displacement error estimates from such tests are limited to precision, as slight shifts in sample position from vibration of the scanner may result in an unknown but true shift in the displacement field. The zero-strain test quantifies measurement errors arising from image noise, artifacts, and interpolation errors in the DVC method. Conversely, error estimates arising from artificially shifted datasets derived from a single scan capture only the errors associated with the chosen DVC method's interpolation approach, and its ability to capture larger deformations. It has been found that zero-strain displacement SD is a good surrogate for true measurement error in cases of low to moderate deformation [102].

Many studies to date have focused solely on the measurement error of DVC, reporting zero-strain displacement SD of less than 1/10th of the voxel size for µCT scans [20,21,93,101,103,104]. Because DVC errors are largely dependent on image quality, the choice of imaging method is an important one, also guided by physical constraints and availability. Table 2-1 summarizes the advantages and disadvantages of some of the more common imaging modalities used with DVC. Although lab µCT is by far the most common imaging tool for DVC studies, it may not always be appropriate. To produce the displacement fields in bone samples, external loading rigs must be used. If the specimen itself is also quite large, the overall footprint of the experimental testing setup may exceed what a conventional µCT system can accommodate. In these cases, clinical HR-pQCT scanners may be the only option, due to their wide, open bore. Micro-magnetic resonance imaging (MRI) can achieve suitable resolutions for DVC studies (voxel size <80µm) without subjecting specimens to a radiation dose, though its use is uncommon due to long scan times (> 9 hours) and specimen size restrictions similar to lab µCT [100].

Table 2-1 Summary of different imaging modalities commonly used with DVC, highlighting the advantages and disadvantages associated with each (*Ø* indicates scan diameter, *L* indicates length)

Modality (*Typical scan limitations*)	**Advantages**	**Disadvantages**
Lab µCT *(Ø<80mm, L<120mm, Voxel<10µm)*	• High nominal resolution • Desktop and cabinet units commonly available within bone research labs	• Often restricted for specimen length/volume • Scan times can be very long, and file sizes very large
Synchrotron µCT *(Scan size depends on synchrotron facility and beamline,* *Voxel<1µm)*	• Extremely high resolution • Beamline facilities are designed to be configured for a wide range of experiments, and can accommodate large custom loading rigs	• Access typically requires detailed research proposals and condensed testing/scanning schedules • Requires specially trained personnel • High radiation dose risks locally damaging bone microarchitecture
HR-pQCT *(Ø<140mm, L<240mm, Voxel<41µm)*	• Wide, open-bore scanner can accommodate large, long samples and custom loading rigs • Clinical research tool, easier to access and use than synchrotron facilities	• Image quality (SNR, resolution) is lower than lab or synchrotron µCT • Scanning protocol can produce artifacts between scan blocks, interpreted as displacements by DVC [25,105,106]

To date, HR-pQCT has been used sparingly with DVC studies: only two studies exist, both quantifying local displacements in relatively small scan volumes surrounding femoral implants [24,25]. Internal displacements in large scan volumes have not been investigated. HR-pQCT has high nominal resolution for a clinical tool (<41µm voxel size), but also introduces unique challenges: image quality is poor compared to µCT (e.g., lower signal-to-noise ratio, or SNR), and long scan volumes are corrupted by discontinuities potentially resulting in erroneous displacements in DVC [25,106] which have not yet been addressed. To improve measurement precision and accuracy, past DVC studies have incorporated image denoising filters to increase SNR [95,96]. Relatively simple denoising methods such as Gaussian convolution or median filtering are computationally inexpensive, but do not actively preserve edge information, and may remove or blur details vital for tracking features in DVC. Bilateral filtering improves upon Gaussian by adding a spectral convolution kernel based on intensity differences, to preserve edge information. Other approaches include: non-local means (NLM) denoising, which removes noise by averaging pixels from similar regions of an image [107]; and total variation denoising (TVD), which frames image restoration as a minimization problem, seeking a new image similar to the original but with lower smaller total variation [108]. Image denoising is computationally demanding for large 3D datasets, making it important to weigh the benefits in image quality from different methods against their associated cost. Image filtering has the potential to reduce DVC error with HR-pQCT scans by improving SNR, though it has not yet been investigated. A more thorough analysis of the errors associated with DVC-measured displacements in HR-pQCT scans is required before its use studying large specimens such as the tibia, where errors can compound over the long scan length.

2.4.4 Validation of FE models of bone using DVC

DVC is well suited for use validating predictions from FE models, as it is capable of providing precise measurements of internal bone deformation in a non-invasive manner. The first study to compare FE predictions of internal bone mechanics to experimental measurements from DVC was performed in 2006 by Zauel et al. [21]. Using DVC displacements to replicate boundary conditions (BCs) for µFE models of two trabecular bone cores, excellent agreement was found for displacements (R^2=0.97) in the mechanical testing direction, while the other displacement components were not as well predicted (R^2 of 0.60 and 0.29) [21]. Strains were also investigated but were less reliable as a validation measure due to their increased measurement error (strains, are prone to high errors (hundreds of microstrain) as they must be obtained by numerical differentiation of the already noisy displacement field). Studies since then have focused solely on displacements, achieving similar agreement between µFE predictions and DVC measurements (R^2>0.97, RMSE%<3%) [23,109]. By directly modeling the complex trabecular microarchitecture, µFE models can accurately predict internal bone mechanics. However, achieving similar accuracy with homogenized QCT-FE models is a more difficult task due to the added complexities associated with geometry approximation and indirect modeling of bone anisotropy. Jackman et al. used DVC to investigate the accuracy of displacement predictions from QCT-FE models of human vertebrae, with relatively poor agreement (median displacement error ranging from 12% to 279%); their findings emphasize that accurate predictions of overall bone stiffness/strength do not necessarily imply similar predictive ability for internal structural behaviour [92]. More recent studies validating QCT-FE models of the human scapula obtained excellent agreement for internal displacements [22,110]; though, reaction force predictions were found to depend strongly on the choice of selected E-BMD relationship [22]. To date, no studies have assessed the accuracy of

QCT-FE predictions of internal bone mechanics for the tibia or any other human long bone. With such models becoming more prevalent in the study of OA progression, treatment and mitigation, the lack of a thorough validation study investigating the agreement of internal predictions with experimental measurements represents a gap in the literature that needs to be addressed.

2.5 Summary of the literature

1. Subject-specific finite element models derived from clinical QCT can assist researchers in understanding musculoskeletal diseases like OA, by providing a non-invasive *in-vivo* tool for investigating the mechanical interactions of bone and soft tissue. QCT-FE models also play a role in the development of joint replacements.
2. Experimental validation of current QCT-FE models of the human tibia has been limited to surface measurements such as cortical bone strains and local subchondral stiffness. It is unclear whether these models predict internal bone mechanics of the proximal tibia, and how the choice of E-BMD relationship affects model accuracy.
3. Trabecular bone is inherently anisotropic, optimized to its local loading conditions. Advanced QCT-FE models of the proximal tibia which incorporate spatially varying anisotropy modestly improve the accuracy of predictions of local subchondral stiffness over their simpler isotropic counterparts. Yet, the effect of spatially varying anisotropy on the accuracy of predictions of internal bone mechanics has not been investigated.
4. DVC allows researchers to measure internal bone displacements non-invasively. Previous studies have used DVC to validate µFE models of trabecular bone samples and QCT-FE models of the human scapula and human vertebra. However, no study has yet used DVC to validate a FE model of a long human bone, such as the tibia.
5. While the measurement error of DVC with µCT has been well studied, such scanners have strict limitations on specimen size ($Ø$<80mm, L<120mm). HR-pQCT can accommodate much larger specimens ($Ø$<140mm, L<240mm) but requires compromises in terms of image quality. The displacement error of HR-pQCT based DVC has not been investigated for large scan volumes, which are necessary for the study of human long bones.

CHAPTER 3

3 RESEARCH QUESTIONS & OBJECTIVES

To address gaps in the literature regarding the feasibility of measuring internal displacements in long bones and the validation of QCT-FE models of the tibia, my specific research questions were:

1. What is the error associated with DVC measures of internal bone displacement when using HR-pQCT with long bones and large scan volumes?
2. Which density-modulus relationship(s) and material models result in the most accurate QCT-FE predictions of internal bone displacements and total reaction force?

To answer these questions, my objectives were to:

1. Establish a method for HR-pQCT scan acquisition and subsequent image processing that results in low DVC displacement error for long bones.
2. Apply different density-modulus relationships and material models from the literature to QCT-FE models of the proximal tibia and identify those best predicting experimentally measured internal bone displacements and external reaction forces with highest explained variance and least error.

CHAPTER 4

4 PRECISION OF INTERNAL DISPLACEMENT MEASUREMENTS IN LONG BONES USING HR-PQCT AND DIGITAL VOLUME CORRELATION

4.1 Overview

In this chapter, we used repeated zero-strain HR-pQCT scans and DVC to quantify the precision errors associated with internal displacement measurements in long human bones. Analysis of the displacement fields indicated that displacements greater than 18.9µm (0.46 voxels) can be reliably measured in the tibia, making HR-pQCT a viable imaging modality for the study of internal bone mechanics of long bones. Image denoising was found to have minimal effect on displacement precision using the tested filters and parameters, suggesting that one should carefully weigh any potential improvements in displacement precision against the additional computational expenses of filtering large HR-pQCT datasets.

4.2 Introduction

Traditionally, µCT has been the modality of choice for DVC studies due to its high nominal resolution (voxel size <10µm), low noise and prevalence in research labs worldwide. Various studies have assessed the displacement precision of µCT-based DVC (µCT-DVC), reporting results ranging from 0.008 to 0.05 voxels [20,21,93,103,111]. An inherent limitation of cabinet or desktop µCT systems is their small, closed design which imposes strict experimental constraints. The loading rigs necessary to deform samples take up space, limiting most µCT-DVC studies to smaller, *ex-vivo* specimens such as excised bone cores/cubes [20,23] or small animal bones [112]. Micro-MRI, a non-irradiating 3D imaging method, suffers from similar constraints on specimen size and scan volume [100]. Clinical HR-pQCT scanners, on the other hand, have a large diameter, open-ended bore that can accommodate much longer specimens and the equipment necessary to hold them and apply load. Compared to µCT, HR-pQCT has a poorer nominal resolution (41µm to 82µm voxel) [113] and poorer image quality, as it is intended as a clinical, (*in-vivo)* research tool and prioritizes fast scan acquisition and low radiation dose. Discontinuities in the 3D scans from HR-pQCT have also been reported, caused by the stacking of sequentially acquired scan ‘blocks’ when imaging large volumes [25,105,106]. Only a few studies have utilized HR-pQCT for DVC [24,25], reporting displacement precision errors below 0.1 voxels. However, DVC analyses in these studies were limited to small regions comprised of one or two scan blocks, inter-block displacement errors were not addressed, and the effects of different image denoising methods were not investigated. HR-pQCT may be one of few viable options for the validation of internal displacements in FE models of long human bones, but requires further investigation first.

The primary objective of this study was to establish a method for HR-pQCT scan acquisition and subsequent image processing resulting in precise DVC measures of internal bone displacement in long bones. The secondary objective was to investigate the effects of image denoising methods (median, bilateral, NLM, TVD) on precision errors.

4.3 Methods

4.3.1 Specimens

We acquired five embalmed (formalin-fixed) cadaveric knee joints (2 right and 3 left knees) from the University of Saskatchewan College of Medicine (mean age (SD): 80.2 (14.1) years). Joints were of unknown disease status from 4 donors (3 females and 1 male). We separated each joint, removing the femur, fibula and patella. The tibial compartments were carefully cleaned of all soft tissue (ligaments, meniscus, and cartilage) using a scalpel, revealing the underlying subchondral bone. After cleaning the bone surface, we cut each tibia transversely at the shaft to appropriate length and ‘potted’ by embedding in a polyvinylchloride (PVC) pipe with dental cement

(Denstone). Care was taken to ensure both the medial and lateral compartments were level with the base of the PVC pipe to facilitate even, distributed mechanical loading. A layer of polymethylmethacrylate (PMMA) was added above the dental cement to form a cap and prevent movement of the tibia during curing of the dental cement. Approximately 60mm of each proximal tibia was left exposed for imaging. Additionally, two tee-nuts were embedded in the base of each PVC pot for attachment to a custom loading rig during imaging.

4.3.2 Specimen holder/loading rig

To hold the specimens and perform mechanical testing during image acquisition, we designed and manufactured a custom, radiolucent loading rig (transparent to x-rays from CT systems) (Figure 4-1). The dimensions of the loading rig were constrained to fit inside the bore of a first-generation HR-pQCT scanner (XtremeCT; Scanco Medical AG, Brüttisellen, Switzerland), with a maximum diameter of 176mm. A 1/4in. thick acrylic tube constituted the body of the rig (Figure 4-1), with a special endcap machined with slotted holes. An intermediate aluminum plate attached to the specimens' PVC potting, which formed a simple *x-y* positioning table when attached to the rig via the slotted acrylic endcap. The other end of the tube was fitted with an aluminum flange designed to bolt to the end of an electromechanical actuator (Zwick Z010; ZwickRoell, Ulm, Germany), to allow for remote load application and control. A steel bracket was machined to mount to the end of the actuator, offsetting the load cell and point of load application from its centerline. All components of the rig were designed to withstand 10kN of applied load, the nameplate capacity of the actuator. Solvent was used to fuse the acrylic tube and endcap, and a high strength epoxy was used to attach the flange to the tube.

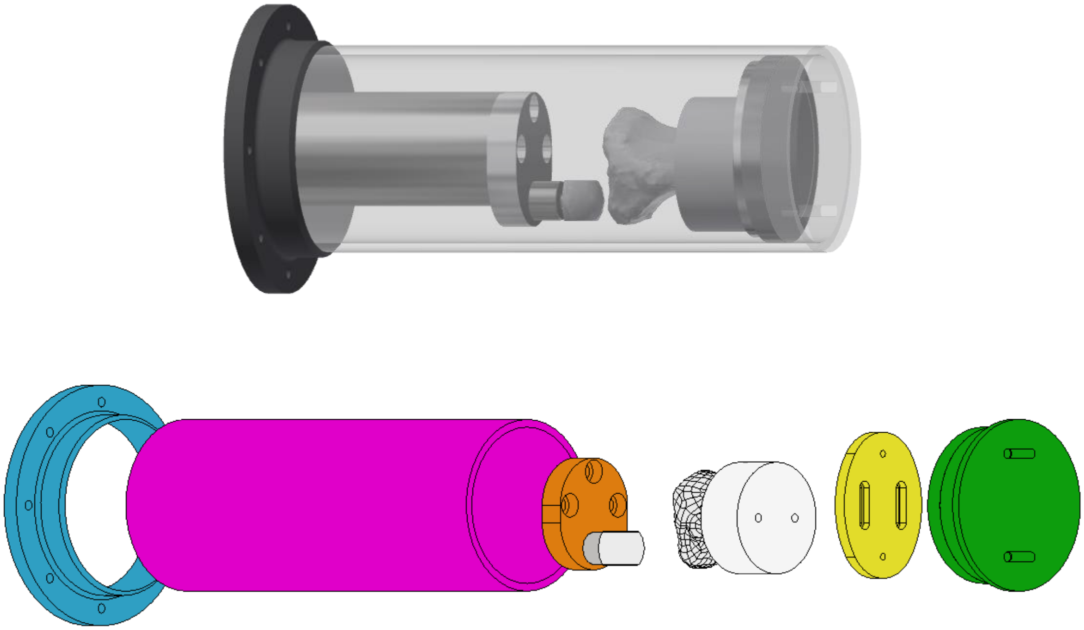

Figure 4-1 3D rendering of the custom loading rig for use with HR-pQCT, in assembled form (top) and in an exploded view (bottom). Shown in blue is the flange to attach to the Zwick actuator, orange is the offset steel bracket, yellow is the aluminum sliding plate, green is the slotted acrylic endcap, and magenta is the acrylic tube.

4.3.3 HR-pQCT image acquisition and scan stitching

We attached the potted specimens to the loading rig (Figure 4-2a) which was then inserted into the bore of the HR-pQCT scanner (XtremeCT I) located in the U of S College of Kinesiology's Laboratory for Imaging Muscle and Bone Structure (Figure 4-2b). Using the Zwick actuator, we applied a 50N preload force to the medial tibial compartment via a composite femoral condyle model (referred to as the indenter). The medial preload was applied to limit specimen motion which might occur during scanning due to scanner vibrations. After initial load application, the specimen was allowed to relax for 15 minutes prior to imaging to minimize motion artifacts from load relaxation. Two zero-strain scans were acquired for each specimen [20] using the HR-pQCT's high resolution mode with an isotropic voxel size of 41µm (60kV tube voltage, 1 mA tube current, 300ms integration time, 3072x3072 pixel image matrix), capturing a region approximately 65mm in length (~1600 slices). No repositioning occurred between scans.

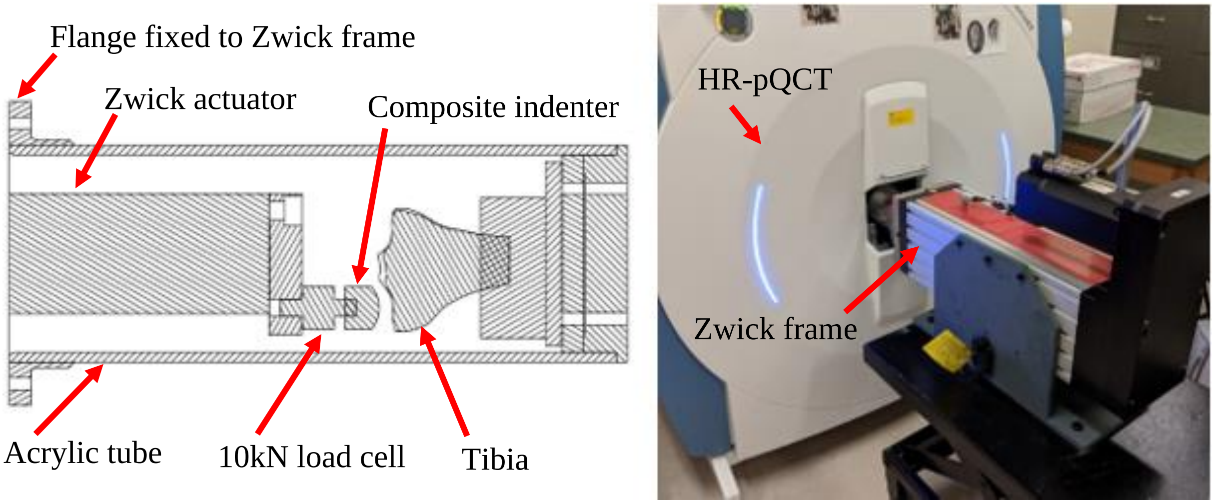

(a) (b)

Figure 4-2 **(a)** Cross-section of the custom offset loading rig with a specimen inserted, **(b)** loading rig attached to the Zwick actuator frame and inserted into the HR-pQCT scanner bore

Like other CT imaging methods, HR-pQCT scans can suffer from artifacts due to hardware imperfections. Beam hardening occurs when the polychromatic x-ray beam passes through the specimen to be imaged and the lower energy photons are attenuated; the exiting photons have a higher mean energy, resulting in reconstructed slices that appear overly dense at the tissue surface [114]. The XtremeCT scanner mitigates beam hardening effects by use of a physical copper and aluminum filter to remove certain x-ray energy bands, along with applying a software correction during scan reconstruction [113]. Ring artifacts were present in the HR-pQCT scans, resulting from defective or poorly calibrated detector elements; these appeared as thin rings ‘cut’ into the image slices, centered about the axis of rotation [114]. After reconstruction, scans were ring-corrected in MATLAB using a wavelet and fast Fourier transform (FFT) destriping method [115].

The artifacts described above are common to all CT imaging systems; however, HR-pQCT scans may also exhibit another artifact when imaging long specimens. With a detector size limited to 220 slices, the HR-pQCT acquires larger scan volumes as a series of sequentially acquired blocks, which are then stacked together after reconstruction. Small errors in the gantry stepper motor positioning can result in misalignments between sequential scan blocks; the standard imaging protocol uses data from the gantry position sensor to align and stack the scan blocks, though small misalignments persist in the reconstructed volumes (Figure 4-3a) and are erroneously interpreted as displacements by DVC. To minimize inter-block displacement errors, we developed a modified scanning procedure, incorporating the following steps:

1. Acquire a series of 220-slice scan blocks, each block overlapping the preceding one by 20 slices (using a custom *OpenVMS DCL* script for batch operation).
2. Reconstruct each scan block using the standard Scanco reconstruction algorithm.
3. Download all scan blocks with MATLAB using the standard File Transfer Protocol (FTP).
4. Correct ring artifacts present in each block by converting the 2D image slices into polar coordinates (turning ring artifacts into vertical stripes) and using a wavelet-FFT destriping method [115].
5. Determine shift between each set of overlapping blocks:
    a. Convolve blocks with a Gaussian filter of SD = 1.5 for noise suppression.
    b. Identify integer shift resulting in maximum phase correlation via FFT.

    c. Perform multiscale sub-voxel registration with linear interpolation, maximizing the normalized correlation coefficient using the Nelder-Mead optimization method [116] and the shift from 5b as a starting point.

6. Shift each ring-corrected block by the optimal value from Step 5 and use linear alpha-weighted blending to combine overlapping regions.

Using the modified scanning procedure, large-volume scans were acquired with no visible inter-block misalignments (Figure 4-3b). We only considered *x*, *y* and *z* translations during the registration process. The addition of rotational degrees of freedom was investigated, however the drastic increases in computation time resulted in no discernable improvements in quality of the final stitched volume.

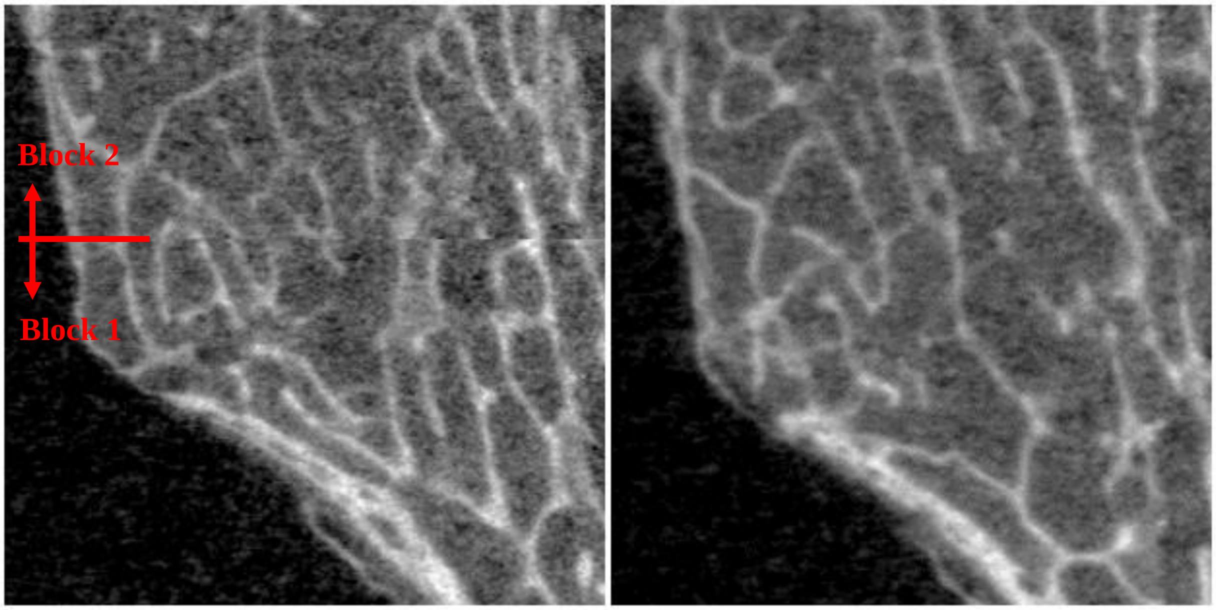

(a) (b)

Figure 4-3 Multi-block scans acquired **(a)** using the standard scanning procedure and **(b)** using the modified procedure via block stitching. The seam between blocks is visible in the standard procedure, but essentially disappears with the modified protocol.

4.3.4 Image post processing

To investigate the effects of noise filtering on DVC measurement precision, we tested several noise reduction methods: a median filter [96]; a bilateral filter; NLM denoising [107]; and TVD [108]. All methods were implemented in MATLAB, and the parameters used are summarized in Table 4-1. To select the parameters, we adopted a simple qualitative approach: beginning with each method's default parameters, we made adjustments to achieve suitable reductions in the SD of uniform image regions (air, marrow) while preserving definition of the edges of the trabecular and cortical bone (minimizing blurring). This method was chosen for simplicity, as we did not have noiseless 'ground truth' images. All filtering was performed on the raw 16-bit signed images.

Table 4-1 Summary of parameters used for denoising of HR-pQCT images prior to displacement field measurement from DVC

Filtering method	**Parameters**
Median	- Kernel radius: 2 voxels
Bilateral	- Kernel radius: 4 voxels - Spatial sigma: 1.0 - Degree of smoothing: 1e8
NLM	- Search window radius: 10 voxels - Comparison window radius: 2 voxels - Degree of smoothing: 350
TVD	- Number of iterations: 50 - Lambda: 0.1

After reconstruction, stitching and filtering, we normalized the 16-bit signed image volumes to 8-bit unsigned values to reduce storage and computational costs for DVC. Values below or above specified cutoffs (0 and 1350mgHA/cm^3) were set to 0 and 255, respectively, while values between the cutoffs were scaled linearly; this was done to maximize contrast between bone and the surrounding marrow and air [20]. The cutoffs were chosen based on the realistic density range for bone tissue: voxels with BMD less than 0 correspond to air or marrow, and voxels with BMD greater than 1350 exceed that of fully mineralized bone and correspond to CT artifacts.

4.3.5 Digital volume correlation

Using *DaVis 10.0* (LaVision GmbH, Göttingen, Germany), a commercial DVC program utilizing a local correlation approach, we obtained displacement fields for each set of zero-strain scans. An initial displacement field with integer precision was obtained using FFT with a subvolume edge length of 128 voxels, which was then refined to sub-voxel precision via a multiscale direct correlation approach. Cubic subvolume widths of 128, 96, and 64 voxels were utilized in succession, followed by a Gaussian-weighted spherical subvolume with a diameter of 48 voxels (no overlap). Within each correlation stage at a given subvolume size, *DaVis'* multipass algorithm was used, a predictor-corrector method that iteratively refines the displacement field [97] and has been shown to decrease measurement error [96].

4.3.6 Statistical analysis

During displacement measurement with the DVC software, we discarded any DVC sample points with a normalized cross-correlation coefficient less than 0.75, as per LaVision's recommendations [97]; this was done to remove poorly correlated (and thus inaccurate) measurement points corresponding to image artifacts or the relatively uniform-intensity indenter. Points with a BVF less than 1%, calculated as the mean BMD at each sample point divided by 1200mgHA/cm^3 [117], were also discarded so as to exclude subvolumes containing only air or marrow from analysis. To estimate the measurement precision of DVC, we calculated the standard deviation of each displacement component (x, y, z) for each zero-strain DVC dataset [20]. Each displacement field contained approximately 13,000 measurement points. The pooled precision for each displacement component was then calculated as the root-mean-square standard deviation (SD_{rms}):

$$SD_{rms} = \sqrt{\frac{1}{n}\sum_{i-1}^{n} SD_i^2}, \tag{4-1}$$

where SD_i is the zero-strain SD of specimen i and n is the number of specimens (5 for this study). We used least significant change (LSC), calculated as 2.77 times SD_{rms} [118], to estimate the minimum displacement that can be measured with 95% confidence.

4.4 Results

For the unfiltered zero-strain HR-pQCT scans, DVC displacement SD was 4.10µm, 5.43µm and 6.82µm in the *x*, *y*, and *z* directions, respectively, corresponding to LSCs of 11.4µm, 15.0µm and 18.9µm (Table 4-2). The application of various denoising filters had little effect on displacement precision, with SD_{rms} ranging from 4.08µm to 4.16µm in the *x*-direction (medial-lateral), 5.38µm to 5.43µm in the *y*-direction (anterior-posterior) and 6.79µm to 6.82µm in the *z*-direction (inferior-superior) (Table 4-2). Histograms of the zero-strain displacement fields were multi-modal, representing multiple superimposed Gaussian distributions (Figure 4-4).

Table 4-2 Zero-strain DVC displacement error estimates in each coordinate direction for different noise filtering techniques. Root-mean-square standard deviation (SD_{rms}) is reported in µm, with the corresponding least significant change (LSC) in parentheses

Filtering	**DVC displacement component**		
	x	*y*	*z*
None	4.10 (11.4)	5.43 (15.0)	6.82 (18.9)
Median	4.16 (11.5)	5.38 (14.9)	6.80 (18.9)
Bilateral	4.14 (11.5)	5.38 (14.9)	6.82 (18.9)
NLM	4.09 (11.3)	5.41 (15.0)	6.81 (18.9)
TVD	4.08 (11.3)	5.39 (14.9)	6.79 (18.8)

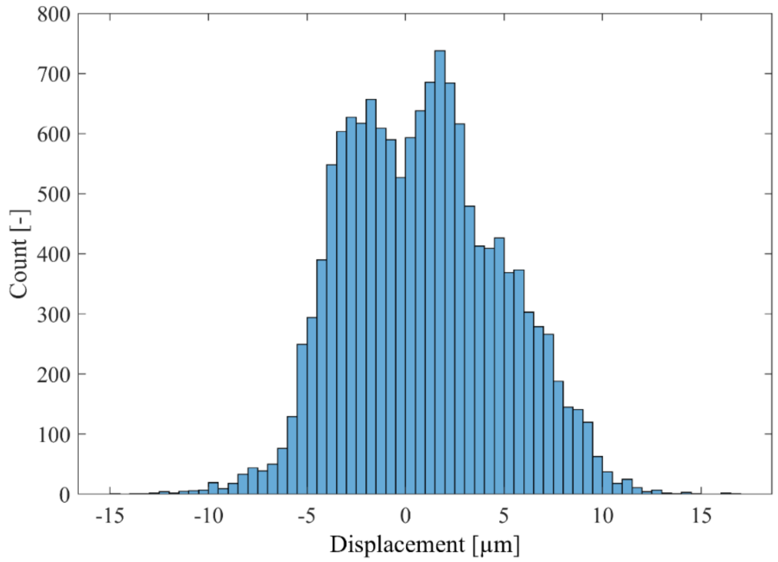

Figure 4-4 Representative histogram of the displacement field measured by DVC for a set of zero-strain HR-pQCT scans, using the modified scanning procedure

4.5 Discussion

This study evaluated the measurement error of DVC-derived displacement measurements obtained from zero-strain HR-pQCT scans of the human tibia. Overall, displacement errors were satisfactorily low (SD_{rms}<0.17 voxels, LSC<0.46 voxels), and indicate that HR-pQCT based DVC can capture internal displacement measurements with sub-voxel precision, accurate enough for studies of long human bones. We also investigated the effects of different denoising filters. The results of this study suggest that the potential benefits of applying image denoising filters to HR-pQCT scans prior to use with DVC are minimal, and may not be worth the additional computational effort. Reductions in displacement SD_{rms} from denoising were all lower than 0.1μm, representing a negligible improvement.

Our DVC displacement SD_{rms} (0.17 voxels), relative to voxel size, is higher than nearly all the values reported in the literature for µCT-based DVC (0.008 to 0.05 voxels) [20,21,93,103,111]; this is expected due to the superior spatial resolution and SNR of µCT. To achieve a nominal isotropic voxel size of 41µm, the first-generation HR-pQCT scanner had to operate in a non-standard scanning mode, whereby the CCD array used 1x1 binning (the standard patient protocol uses 4x1 binning, averaging the results of four detector elements to form one pixel, reducing noise). Two studies have reported displacement SD for HR-pQCT based DVC, with values lower than 0.1 voxels [24,119]. However, neither study addressed the inherent difficulties of DVC with large-volume scans. The error estimations of Basler et al. were based on virtually translated and deformed datasets rather than repeated scans [24], thus providing an unrealistic best-case scenario for DVC by eliminating error from image noise, ring artifacts and inter-block errors. Although Rapagna et al. addressed some of these shortcomings by measuring DVC displacement SD for repeated scans, the analysis was limited to small cubic VOIs of edge-length 15mm [25] and compounded errors from multiple scan block boundaries were not present. Furthermore, the lower relative error of the previous studies (with respect to voxel size) was likely influenced by their use of the standard scanning resolutions with 4x1 binning and second-generation hardware (vs. our first-generation hardware).

We adopted a modified scanning procedure for this study to reduce the inter-block discontinuities present in large-volume HR-pQCT scans. While visual misalignments at the block boundaries were effectively eliminated by the registration and stitching process (Figure 4-3), small discontinuities persisted in the DVC-measured displacement fields. Analysis of the displacement histograms revealed multi-modal distributions, with peaks separated by ~5µm, which represented inter-block errors up to 0.125 voxels (Figure 4-4). In contrast, large-volume scans acquired without the modified scanning procedure exhibit much larger inter-block errors, between 0.5 and 1.0 voxels [106]. Within individual scan blocks, errors were normally distributed. The displacement SD was consistently highest in the *z*-direction, followed by the *y*-direction and then the *x*-direction – this may be a product of the minimization approach used during image registration. To identify the optimal shift vector between two blocks, MATLAB's implementation of the Nelder-Mead simplex method was used, passed parameters in the order of *x*, then *y,* then *z.* It is possible that rearranging the order in which the parameters were passed for optimization may have an effect on which shift component identified was most optimal. It should also be noted that scans from the newer, second-generation HR-pQCT are afflicted by inter-block errors as well [105]; given their small absolute size it is unlikely that hardware improvements alone could eliminate these errors, making registration and stitching methods like the one described here necessary.

Our findings regarding the lack of effect from image denoising agree with those of Fernandez et al. [96]. Despite improvements in overall image quality, denoising had little effect on the displacement error from DVC. Our relatively large subvolume size for DVC (48 voxels) makes measurement more robust and less sensitive to image noise; displacement and strain measurements from smaller subvolumes are likely a better candidate for image denoising, as they experience higher precision errors due to sampling fewer neighboring voxels at each measurement point [101]. Furthermore, while denoising filters target random and normally distributed noise, the largest errors in our datasets originated from the inter-block misalignments. Therefore, any reductions in the errors associated with image noise are likely to pale in comparison to the remaining errors from the registration and stitching process, which are not random and are not removed by denoising. To remove such errors, post-processing of the DVC displacement fields may have potential; though, more complex filtering techniques would be required as conventional image and data denoising techniques target random rather than systematic error. Combined wavelet and FFT filtering can be used to correct ‘banded’ and striped datasets [115], much like the ring artifact correction technique used with the reconstructed HR-pQCT scans in this study. In order to use such an approach with DVC data, however, a much finer displacement field (via smaller or overlapping subvolumes) would be required to better localize the step discontinuities.

This study has several strengths which require consideration. First, rather than constrain the analysis to regions within scan blocks to avoid inter-block errors [25], we adopted a modified scanning procedure to mitigate these errors and use the full scan length (~60mm here) for displacement measurement with DVC. For long human bones such as the femur or tibia, HR-pQCT may be the only viable imaging modality that can provide sufficient resolution for DVC analyses, allowing for comparisons to FE model predictions for validation purposes. Other modalities such as SR-µCT are not as readily available and may induce specimen damage via high radiation doses [120]. Secondly, the registration and stitching procedure outlined here is fully automatic and can be directly implemented in the scan acquisition pipeline with no additional operator intervention. The initial, coarse FFT registration followed by the multiscale approach is robust and does not get stuck on local minima. Thirdly, four fundamentally different image filtering approaches were tested, providing a more rigorous investigation of the effects of image denoising on DVC precision than the study of Fernandez et al., which tested only two [96].

There are several limitations of the current study that need to be addressed. First, by only assessing measurement error based on zero-strain scans, our estimates represent a lower bound on the displacement errors that may be present in strained bone samples. A recent study by Comini et al., however, suggests that in cases of moderate applied strain, the error estimates provided by a zero-strain analysis are reasonable [102]. Secondly, the HR-pQCT scanner used in this study was a first-generation XtremeCT, which is being phased out by its successor, the XtremeCT II. The new, second-generation of HR-pQCT is more ideally suited to DVC studies, offering a higher nominal resolution and accommodating specimens of larger diameter and length [121]. It would therefore be beneficial to repeat this study with a XtremeCT II scanner to evaluate DVC displacement error. Thirdly, our registration approach during image stitching was limited to three translational DOFs and a linear interpolation scheme. Including rotational DOFs and employing cubic or spline interpolation may lead to further reductions in inter-block errors and warrants future investigation. The decision to omit these in the current study was based on computational costs, which grow quickly when working with large datasets. Finally, each denoising method used here was only tested with one set of parameters, chosen based on visual assessment of image quality. Optimal filter parameters selected by a more rigorous approach may yield different results, and improve DVC displacement precision.

4.6 Conclusion

This study is the first to report the precision errors associated with DVC measured displacements of large analysis regions, such as in long bones. Displacement SD_{rms} ranged from 4.08μm to 6.82μm, corresponding to LSCs ranging from 11.3μm to 18.9μm. The application of different image denoising filters had minimal effect on displacement errors, due to the much larger inter-block errors associated with the large-volume scanning protocol. Our results suggest that HR-pQCT is a viable imaging modality for use with DVC for the study of internal displacements in long specimens as it was able to reliably measure displacements with sub-voxel precision errors.

CHAPTER 5

5 EXPERIMENTAL VALIDATION OF FINITE ELEMENT MODELS OF THE PROXIMAL TIBIA FOR INTERNAL DISPLACEMENTS AND EXTERNAL REACTION FORCES USING DIGITAL VOLUME CORRELATION: THE EFFECT OF ASSIGNED MATERIAL PROPERTIES

5.1 Overview

This chapter describes our experimental validation of QCT-FE models for predictions of internal bone displacements and net reaction forces at the human proximal tibia. We tested different combinations of density-modulus relationships for trabecular and cortical bone, considering both isotropic and anisotropic material properties, to investigate the effects of assigned material properties on FE predictions of displacements and reaction forces. The combinations of trabecular and cortical models were identified which best predicted experimentally measured internal bone displacements and external reaction forces, with highest explained variance and least error.

5.2 Introduction

Subject-specific FE models of the proximal tibia have been experimentally validated by comparison of FE predictions to measurements of cortical bone strains [63], local compressive stiffness [18] and torsional stiffness/failure load [8]. The combination of E-BMD relationships from the literature that best predict subchondral stiffness with lowest error have been identified [18], and optimized relationships and material models have been proposed to further improve model predictions [19,78]. However, it is unclear if the optimal E-BMD relationships and material models identified for models predicting subchondral stiffness also predict internal bone mechanics such as bone displacement. To date, a few studies have used DVC to compare experimental internal displacements to QCT-FE predictions for the human scapula [22,110] and human vertebra

[92], but long bones such as the tibia have not yet been investigated using DVC and pose additional challenges due to their larger size. Using the methods introduced in Chapter 4 for large-volume HR-pQCT scanning and subsequent DVC analysis, internal displacements can be measured with low error, making a DVC validation study of QCT-FE models of the proximal tibia feasible.

The objective of this study was to apply different cortical and trabecular models from the literature to QCT-FE models of the proximal tibia and identify the relationship(s) that best predicted experimentally measured internal bone displacements and external reaction forces with highest explained variance and least error.

5.3 Methods

5.3.1 Specimens

For this study, we used the same five cadaveric tibiae described in the previous chapter.

5.3.2 Mechanical testing and HR-pQCT scanning

During mechanical testing and scanning, we fixed each sample in the radiolucent loading rig described earlier in Section 4.3.3 and inserted it into the HR-pQCT scanner bore. We then applied a 50N compressive load to one of the tibial compartments via the Zwick electromechanical actuator and the composite indenter. After waiting 15 minutes to allow for load relaxation to occur, we acquired a scan of the full specimen using the proposed large-volume HR-pQCT scanning methodology described in Section 4.3.3 (Figure 5-1a). Next, we applied compressive displacements of ~0.5, 1.0 and 1.5mm to the tibial compartment in succession. After each load increment, following a 15-minute wait for load relaxation, an HR-pQCT scan was acquired (Figure 5-1b). After the relaxation period, which allowed for stress relaxation [122,123] and slipping at the indenter/bone interface to equilibrate, no further reductions in load were observed during scanning. The loading protocol was repeated for both the medial and lateral compartments of all five specimens. If at any point during load application the force-displacement curve indicated yield/fracture (reduction in applied load), we stopped testing for that specimen and used only the data acquired prior to fracture (previous load steps) for further analysis. Two specimens experienced local failure during one of the load steps, limiting data collection to the previous load steps. As well, inspection of the HR-pQCT scans revealed that a few of the lowest compression load steps did not achieve sufficient contact between the indenter and the subchondral surface, resulting in low applied loads and very local deformation – we excluded these tests from analysis. Ultimately, mechanical testing data and scans were acquired for a total of 21 load steps representing all five specimens (minimum 2 load steps per specimen).

5.3.3 Digital volume correlation

Using the DVC methodology described in the previous Chapter (Section 4.3.5), we obtained experimental displacement fields (Figure 5-1c) for each tibia compartment. The deformed HR-pQCT scan for a given load step was compared directly with that compartment's initial zero-strain scan, rather than the previous load step, to avoid propagation of displacement errors. Poorly correlated sample points with a normalized cross-correlation coefficient less than 0.75 during DVC were excluded [96,97]. In addition, we used a normalized median test to identify and remove outliers from the measured displacement fields [97,124]. At each point, a 5x5x5 voxel VOI was used to calculate the median residual of the displacement field, U_m. A residual vector was obtained by subtracting the VOI's median from every point within the VOI and taking its absolute value. The normalized residual of the central point of the VOI, r_0, was then calculated as

$$r_0=\frac{|U_i-U_m|}{r_m+\varepsilon}, \qquad 5\text{-}1$$

where r_m was the median of the residual vector, and ε established a minimum normalization level (in this case, 0.1 voxels, a level appropriate for the normal fluctuation of cross-correlation data [124]). DVC sample points with a value of r_0 greater than 5 were removed, between 10-50 points per DVC dataset. The points removed corresponded to sample points at the bone surface, with subvolumes partially enclosing air, soft tissue or the indenter, resulting in erroneous displacements.

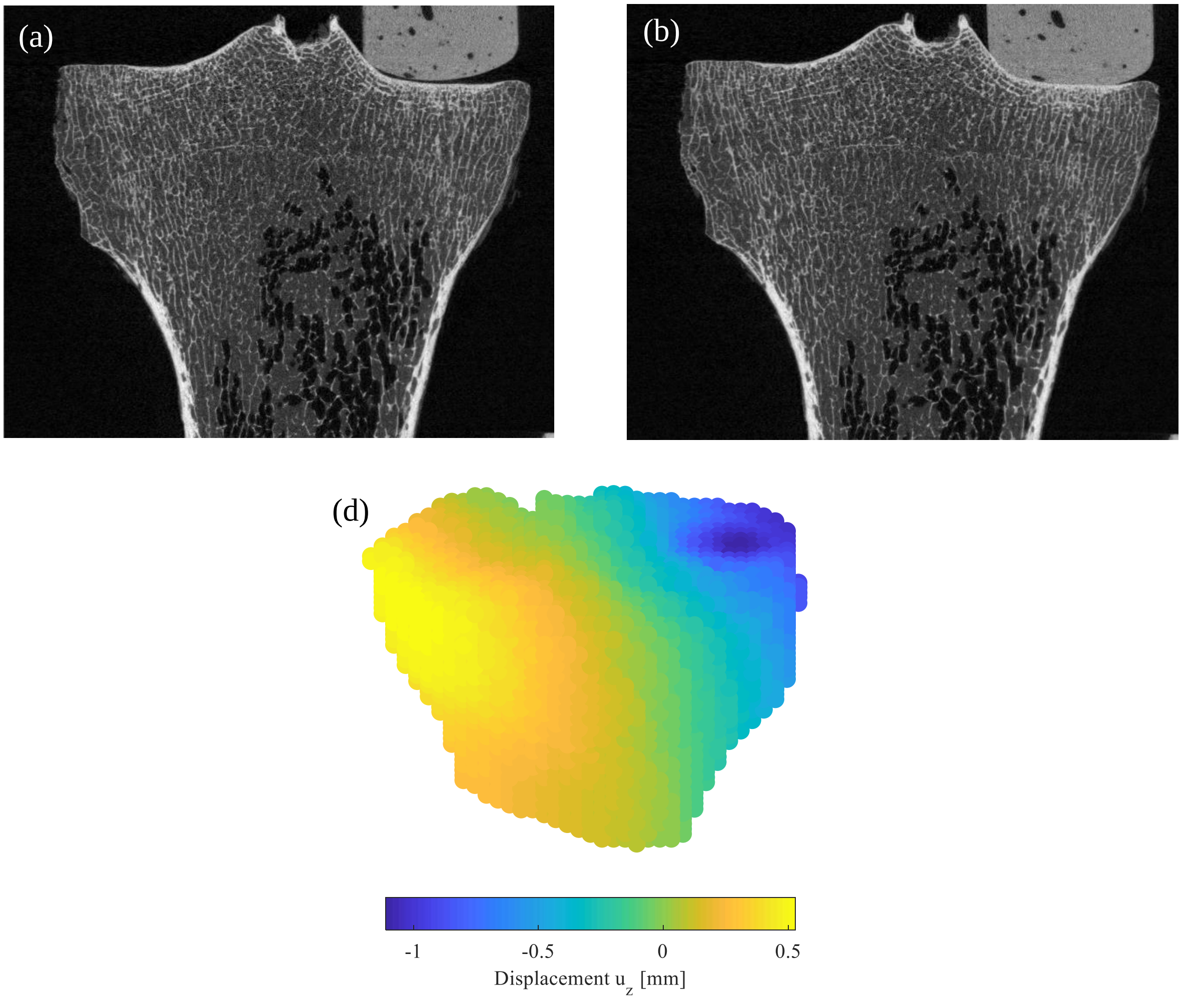

Figure 5-1 Process for digital volume correlation of mechanically tested proximal tibia. A reference HR-pQCT scan is acquired with no applied deformation (a). After applying a compressive load and allowing suitable time for relaxation, a second scan is acquired in the deformed configuration (b). Using *LaVision's DaVis* software, 3D displacement fields are measured with spherical subvolumes of diameter 48 voxels (c).

5.3.4 QCT approximation

While HR-pQCT can resolve trabecular bone's microarchitecture, its clinical use (*in-vivo*) is limited to small sections of bone (~10mm thick) due to long scan times (exceeding one hour), sensitivity to motion artifacts, and elevated radiation dose associated with large scan volumes. Therefore, for clinical relevance, lower resolution QCT scans were simulated from the acquired HR-pQCT scans using a downsampling approach. This approach avoided additional data collection efforts for separate QCT scanning, as well as errors associated with registering separate HR-pQCT and QCT scans (which could result in comparisons between incorrect regions in the FE models and DVC displacement fields). For each compartment, we convolved the initial zero-strain HR-pQCT scan with an estimate of a clinical QCT scanner point-spread-function (PSF) in MATLAB. The PSF was approximated by a 3D Gaussian, defined by its full width at half maximum height (FWHMH) using values reported in the literature for a Toshiba Aquilion 64 scanner [125]. Downsampling was performed using a simple averaging filter to achieve a final isotropic voxel size of 0.5mm (Figure 5-2a). After downsampling, we added Gaussian noise to achieve similar image quality to clinical QCT [76].

5.3.5 Finite element modeling

5.3.5.1 Geometry and mesh generation

Using MATLAB, we generated initial segmentations of the tibia geometry automatically. A global threshold was applied to the QCT images to mark regions of bone (BMD>150mgHA/cm^3). A second volume was created using a local SD filter. From the SD volume, the indenter could be segmented out due to its uniform intensity distribution and thus low SD – regions with SD lower than 60mgHA/cm^3 were removed. This step was necessary as the indenter had similar imaged density to the surrounding bone, making removal by thresholding of the QCT volume alone challenging. We isolated bone from the surrounding air and indenter by taking the binary intersection of the QCT and SD segmentations. Connected components labelling (connectivity of 6) was used to select the largest single component, the bone, and holes were filled using MATLAB's *imfill* function. Finally, the automatically generated segmentations were imported into the *Medical Imaging Interaction Toolkit (MITK 2018.04.2)*, where we made manual corrections with a digital stylus (Figure 5-2a).

Binary segmentations were imported into MATLAB, where we used a custom program to generate voxel-based FE meshes. Each bone voxel was converted into a linear, hexahedral (8-node) finite element with side lengths of 0.5mm. Only the regions of bone not embedded in the dental cement potting were modelled. The element connectivity and nodal coordinate arrays were stored for use during the solution process and later analysis. An element properties array was also created to store the derived mechanical properties of each element. Each model consisted of approximately 750,000 to 1,000,000 elements. To test convergence of FE models, we also created models with a 0.35mm voxel size. We found no changes in FE and DVC comparisons when using the smaller voxel size, therefore the 0.5mm voxel was considered converged and used for the remainder of this study.

5.3.5.2 Material properties assignment

Prior to calculating material properties, the QCT scans needed to be converted from their native intensity scales to BMD. Although the XtremeCT has an internally stored calibration equation for the standard scanning protocols (which is regularly checked for accuracy with daily quality control tests), it was necessary to measure a new one for the higher resolution scan protocol and to account for beam hardening from the loading rig's acrylic tube. We placed the calibration phantom, containing four rods of known density, inside the loading rig used during mechanical testing and scanned with HR-pQCT. After downsampling the phantom scan with the methods described in Section 5.3.4, we used linear regression to create a new linear calibration equation. All QCT scans were then converted to BMD_{HA} (g/cm^3) using this equation.

To evaluate the dependence of model accuracy on the assigned material properties, we generated QCT-FE models using combinations of seven different trabecular-specific E-BMD relationships and two cortical-specific relationships (Table 5-1) for converting imaged density to elastic modulus. Trabecular and cortical bone were separated by a simple threshold of 1.0g/cm^3 apparent density (except for models using the relationships of Nazemi et al., where we used a threshold of 0.5g/cm^3 BMD_{K2HPO4} [19]). Formulae from the literature were used to convert imaged BMD_{HA} to the other densitometric measures required by some of the E-BMD relationships: ash density (ρ_{ash}), apparent density (ρ_{app}), real density (ρ_{real}), bone volume fraction (BV/TV) and dipotassium phosphate BMD (BMD_{K2HPO4}) (Table 5-2). All density measures were in g/cm^3. We assigned elastic modulus directly to each element, assuming isotropic material properties with a Poisson's ratio of 0.3 (Figure 5-2b).

Table 5-1 Density modulus relationships from literature for trabecular and cortical bone, developed from samples of the human tibia or pooled from multiple human anatomical locations

Relationship	**Bone tissue**	**Anatomical location**	**E (MPa)**
Anderson et al., 1992 [71]	Trabecular	Proximal tibia	$3890\rho_{dry}^{2}$
Goulet et al., 1994 [66]	Trabecular	Pooled	$6310(BV/TV)^{2.1}$
Hodgskinson & Currey, 1992 [126]	Trabecular	Pooled	$3311\rho_{dry}^{1.66}$
Keller, 1994 [67]	Both	Pooled	$10500\rho_{ash}^{2.57}$
Linde et al., 1992 [127]	Trabecular	Proximal tibia	$4778\rho_{app}^{1.99}$
Nazemi et al., 2017 [19]	Trabecular	Proximal tibia	$820BMD_{K_2HPO_4}$
Nazemi et al., 2017 [19]	Cortical	Proximal tibia	$31360BMD_{K_2HPO_4}^{3}$
Rho et al., 1995 [69]	Trabecular	Proximal tibia	$6570\rho_{app}^{1.37}$
Rho et al., 1995 [69]	Cortical	Tibial shaft	$13000\rho_{app} - 3842$
Snyder & Schneider, 1991 [128]	Cortical	Tibial shaft	$3891\rho_{app}^{2.39}$

Table 5-2 Equations from the literature for converting between different densitometric measures

$\rho_{ash} = 0.55\rho_{app}$	Helgason et al., 2008 [13]
$\rho_{ash} = 0.597\rho_{dry}$	Keyak et al., 1994 [129]
$\rho_{ash} = 0.877BMD_{HA} + 0.0633$	Keyak et al., 2005 [130]
$\rho_{real} = 1.8\text{g/cm}^3$	Carter and Hayes, 1977 [131]
$\rho_{app} = \rho_{real} \times BV/TV$	Helgason et al., 2008 [13]
$BMD_{K_2HPO_4} = 0.958BMD_{HA} + 0.0653$	Derived for this study

In addition to the isotropic QCT-FE models derived from E-BMD relationships in the literature, we created models that accounted for the spatial variation of anisotropic material properties in the trabecular bone. Local fabric eigenvalues were calculated for each element from the GST [75] based on a 9x9x9 voxel VOI and 6th order centered finite difference for local intensity gradients [76]. Using Cowin's fabric-elasticity equations [77] and the optimal coefficients determined by Nazemi et al. [76] (Table 5-3), we then calculated each element's unique material stiffness matrix. Cortical bone was modelled with one of the two chosen cortical relationships in Table 5-1, assuming uniform anisotropy and orientation [8,63,70]: transverse and shear moduli were calculated as fractions of the on-axis (axial) elastic modulus, E_3, (E_1=0.574E_3, E_2=0.577E_3, G_{12}=0.195E_3, G_{13}=0.216E_3, G_{23}=0.265E_3); and Poisson's ratio in each plane was assumed to be constant (v_{12}=0.427, v_{23}=0.234, v_{31}=0.405). We identified the optimal bone tissue elastic modulus (E_t) for use with the fabric-elasticity equations by minimizing the leave-one-out cross-validation (LOOCV) RMSE via the Nelder-Mead simplex optimization method [78,116].

Table 5-3 Constants for determining material stiffness entries for spatially varying anisotropic trabecular bone using the Cowin fabric-elasticity equations, with an exponent *p* of 1.1 [78].

	k_1	k_2	k_3	k_4	k_5	k_6	k_7	k_8	k_9
a	20.1	53.6	-182.4	70.2	39.7	-32.4	24.2	-44.9	20.7
b	132.0	364.5	-1177.5	303.3	660.6	816.5	-632.5	1050.2	-439.8

5.3.5.3 Boundary conditions (BC)

To best replicate the experimental conditions during mechanical testing, we derived displacement BCs from the DVC-measured displacement fields [20,23]. All nodes lying on the distal surface of the models were assigned BCs by trilinear interpolation of the DVC displacement field. To identify the BC nodes on the proximal end of the models, we used manual segmentation to select all bone voxels that were in direct contact with the indenter at the current load step. By subtracting the DVC-measured displacements of these voxels, their original locations prior to loading could be determined. DVC-driven BCs were then assigned to any surface nodes that fell within the contact region identified (Figure 5-2c).

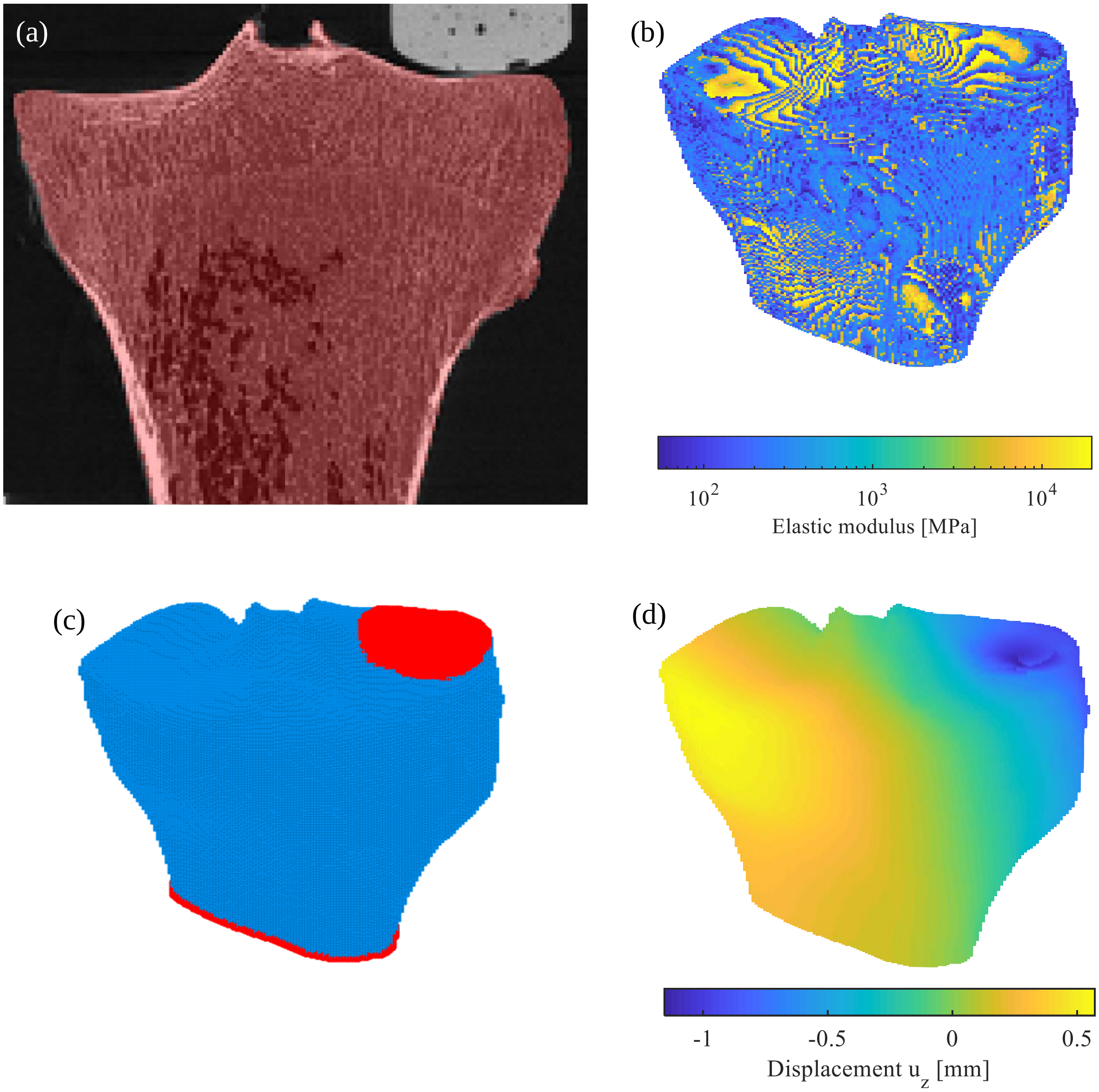

Figure 5-2 The workflow for QCT-FE model creation and solution. The HR-pQCT scans were downsampled to create simulated QCT scans and bone geometry was defined by minimal manual corrections to automatic segmentations (a). A voxel-based mesh was generated by converting each QCT voxel to an element, assigning material properties derived from E-BMD relationships (b). All distal surface nodes as well as nodes which contacted the indenter were assigned displacement boundary conditions derived from DVC (c). FE-predicted displacement fields were obtained using a custom EBE solver in MATLAB (d).

5.3.5.4 Model solution

All QCT-FE models were treated as linearly elastic and solved using our custom EBE solver written in *C++* and interfaced with MATLAB (Figure 5-2d). To utilize all processor cores, we used *OpenMP* preprocessor directives. During the solution process, the global stiffness matrix was never assembled, and an iterative PCG method was implemented with a diagonal preconditioner [53]. Our decision to use an in-house solution rather than a commercial FE software package was motivated by speed and memory consumption. A recent study using the commercial software ABAQUS to solve voxel-based FE models of the proximal femur reported solution times of 3.5 hours for one million elements on a modern desktop workstation, using 128GB of memory [132]. In the present study, our QCT-FE models took less than one minute to solve on average and consumed only 1.5GB of memory, on the same workstation. Comparative analyses of multiple test cases indicated that the in-house program used here provided comparable results to commercial FE software, with differences less than 0.5% in displacement and reaction force outcomes. By using a custom solver, our modeling process was streamlined: meshing; material properties assignment; interpolation of DVC displacements to BCs; FE solving and statistical analysis were all done in the same program without the need to rewrite input files for the FE program, automating the process and eliminating the need to move between programs.

5.3.6 Outcomes

5.3.6.1 Displacements

We paired FE-predicted displacements with DVC measurements by 3D Gaussian-weighted averaging of all FE nodal displacements in a 1mm radius of the DVC measurement points to match the spatial resolution of the DVC grid [92]. Any measurements points within 2mm of a boundary condition node were removed from the analysis. This was done to remove the influence of the displacement-driven BCs on the linear regression results, as nodes in their immediate vicinity would closely match DVC results regardless of selected cortical and trabecular model. After pairing DVC and FE, we removed outliers by identifying any points with Cook's distance greater than 5 times the specimen mean [109]. Less than 4% of total DVC comparison points were removed, leaving 270,000 points for each tested combination of trabecular and cortical models.

5.3.6.2 Reaction forces

During mechanical testing, we defined the experimental reaction forces as the relaxed load prior to HR-pQCT imaging [22], measured by the load cell connected to the Zwick actuator. FE-predicted reaction forces were calculated by summing all resultant nodal loads on the distal surface. We also summed the nodal loads on the proximal surface (loaded by the indenter) separately for comparison to the distal reaction forces, to ensure equilibrium.

5.3.7 Statistical analysis

We used linear regression for assessing agreement between FE-predicted and DVC-measured displacements. Variance in DVC-measured displacement predicted by FE was assessed via coefficients of determination (R^2). To determine if the slope and intercept differed from 1 and 0, respectively, we used students t-tests with a 95% confidence interval.

To evaluate accuracy, we calculated RMSE and RMSE% between FE-predicted and experimentally measured displacements. RMSE was calculated using the following formula:

$$RMSE=\sqrt{\frac{1}{n}\sum_{i=1}^{n}\left(u_{DVC,i}-u_{FE,i}\right)^{2}}, \qquad 5\text{-}2$$

where n was the number of measurement points. As well as calculating RMSE for the individual displacement components, we calculated overall RMSE as the RMS of the Euclidean norm error between DVC and FE at each comparison point. RMSE% for each coordinate direction was obtained by dividing RMSE by that component's largest absolute value experimental measurement, while overall RMSE% was obtained by dividing overall RMSE by the largest Euclidean norm experimental measurement (magnitude from x, y and z displacements). We also constructed Bland-Altman plots to assess agreement and identify mean bias with 95% limits of agreement (LOA) for the displacement difference, calculated as [FE – DVC]. FE-predicted and experimentally measured reaction forces were compared in a similar manner.

5.4 Results

5.4.1 Internal bone displacements

Isotropic QCT-FE models were able to explain >98.6% of the variance in displacement (Table 5-4). Normalized RMSE% between DVC-measured and FE predicted displacements ranged from 4.03% to 4.38% (Table 5-4). We obtained similar results for models using a uniform orthotropic model (constant anisotropy, orientation) for both trabecular and cortical bone (*not reported*). Incorporating spatially varying trabecular anisotropy via Cowin's fabric-elasticity equations offered modestly improved results (R^2:>0.987; RMSE%:3.87-3.88%) (Table 5-5). Here the optimal trabecular tissue modulus for Cowin's fabric elasticity equations was 3.3GPa when used with the cortical model of Rho et al., and 3.6GPa for Snyder & Schneider.

For both isotropic and anisotropic modeling approaches, the slope and intercept of the predictions differed from 1 and 0, respectively, for all directions. Bland-Altman plots indicated no mean bias for the x, y and z-directions. However, there was a proportional bias for the x-direction, illustrating an under-estimation of displacement offered by FE. All linear regression and Bland-Altman plots were nearly identical visually, therefore only those for the optimal relationship of Cowin and Rho et al. are shown (Fig. 5-3).

Table 5-4 Linear regression results comparing FE-predicted and DVC-measured displacements for the isotropic trabecular and cortical models tested. Slopes and intercepts differing from 1 and 0, respectively, are bold ($p < 0.05$).

Cortical model	**Trabecular model**	**Slope**			**Intercept [μm]**			**R^2**			**RMSE%**			
		UX	**UY**	**UZ**	**UX**	**UY**	**UZ**	**UX**	**UY**	**UZ**	**UX**	**UY**	**UZ**	**All**
Rho et al.	Anderson et al.	**1.12**	**1.06**	**1.01**	**-3.50**	**2.14**	**17.0**	0.997	0.987	0.989	3.59	2.74	2.27	4.08
	Goulet et al.	**1.12**	**1.06**	**1.02**	**-3.80**	**1.81**	**15.6**	0.998	0.987	0.989	3.58	2.79	2.22	4.05
	Hodgs. et al.	**1.12**	**1.06**	**1.01**	**-3.29**	**1.94**	**17.0**	0.997	0.988	0.990	3.63	2.73	2.26	4.09
	Keller	**1.12**	**1.05**	**1.02**	**-4.05**	**1.87**	**15.8**	0.997	0.986	0.989	3.57	2.83	2.26	4.07
	Linde et al.	**1.12**	**1.06**	**1.00**	**-3.33**	**2.23**	**18.0**	0.997	0.988	0.989	3.61	2.73	2.33	4.12
	Rho et al.	**1.12**	**1.06**	**0.99**	**-2.62**	**1.30**	**19.9**	0.997	0.988	0.989	3.76	2.75	2.46	4.29
Snyder & Schneider	Anderson et al.	**1.12**	**1.06**	**1.00**	**-3.41**	**2.27**	**17.9**	0.997	0.988	0.989	3.62	2.74	2.32	4.12
	Goulet et al.	**1.12**	**1.06**	**1.01**	**-3.73**	**2.10**	**16.3**	0.997	0.987	0.989	3.58	2.76	2.24	4.06
	Hodgs. et al.	**1.12**	**1.06**	**1.00**	**-3.20**	**1.99**	**17.9**	0.997	0.988	0.989	3.66	2.73	2.31	4.15
	Keller	**1.12**	**1.06**	**1.01**	**-3.97**	**2.20**	**16.4**	0.997	0.986	0.989	3.56	2.80	2.28	4.07
	Linde et al.	**1.12**	**1.06**	**1.00**	**-3.22**	**2.26**	**19.0**	0.997	0.988	0.989	3.65	2.74	2.39	4.18
	Rho et al.	**1.13**	**1.06**	**0.98**	**-2.47**	**1.00**	**20.8**	0.997	0.988	0.989	3.80	2.79	2.54	4.38
Nazemi et al.	Nazemi et al.	**1.12**	**1.06**	**1.02**	**-3.62**	**0.83**	**13.3**	0.998	0.988	0.990	3.64	2.84	2.09	4.03

Table 5-5 Linear regression results comparing FE-predicted and DVC-measured displacements for the anisotropic trabecular model of Cowin et al., paired with the cortical models of Rho et al. or Snyder & Schneider. Slopes and intercepts differing from 1 and 0, respectively, are bold ($p < 0.05$).

Cortical model	**Trabecular model**	**Slope**			**Intercept [μm]**			**R^2**			**RMSE%**			
		UX	**UY**	**UZ**	**UX**	**UY**	**UZ**	**UX**	**UY**	**UZ**	**UX**	**UY**	**UZ**	**All**
Rho et al.	Cowin et al.	**1.11**	**1.06**	**1.01**	**-3.71**	**1.03**	**13.3**	0.998	0.987	0.990	3.45	2.75	2.08	3.88
Snyder & Schneider	Cowin et al.	**1.11**	**1.06**	**1.01**	**-3.66**	**1.41**	**14.0**	0.998	0.988	0.990	3.43	2.71	2.10	3.87

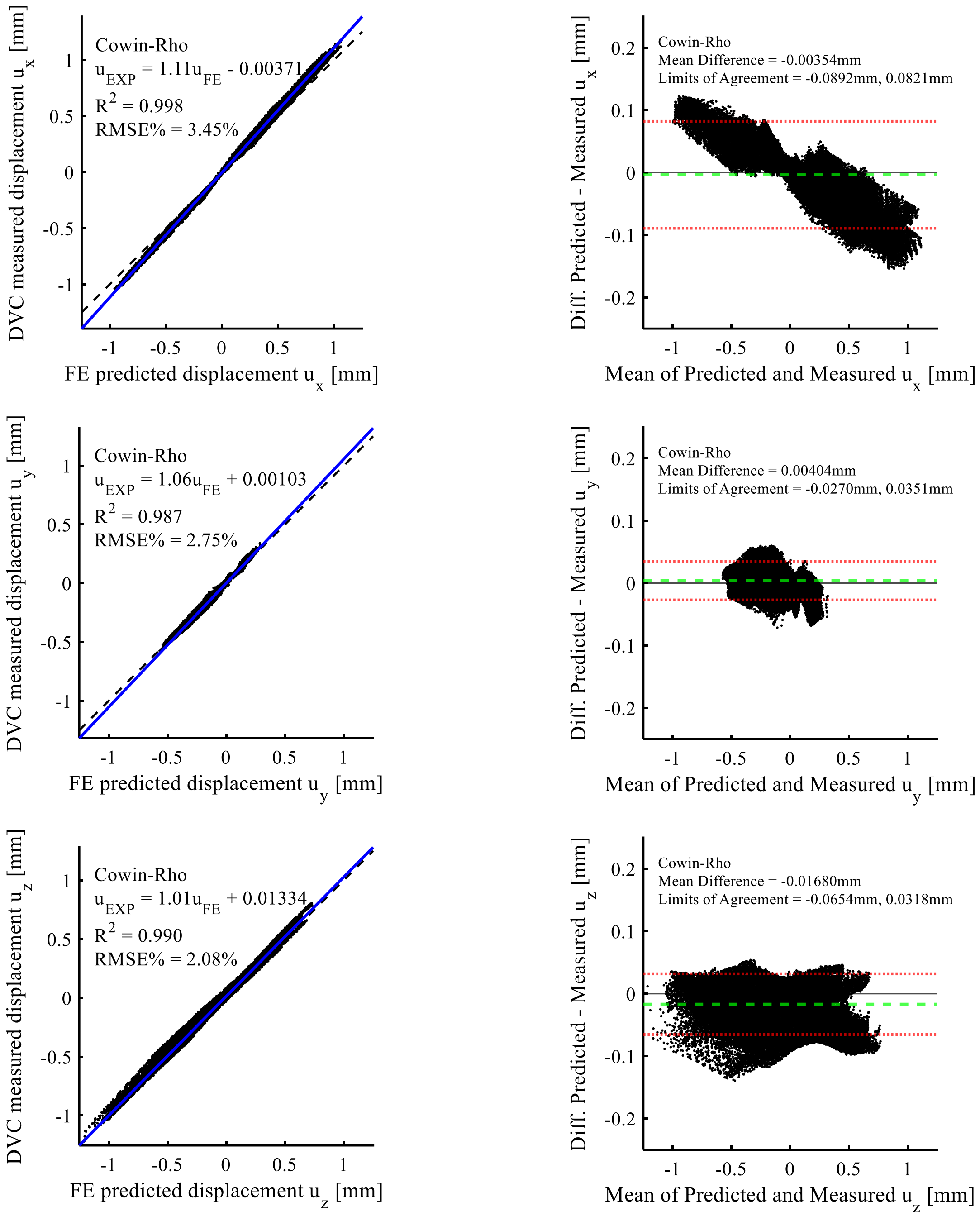

Figure 5-3 Linear regression and Bland-Altman plots comparing FE-predicted and DVC-measured displacements using the fabric-elasticity equations of Cowin for trabecular bone (E_t=3.3GPa) and the relationship of Rho et al. for cortical bone. Dotted black lines are for reference, with a slope of unity and intercept of zero. Blue lines are the linear regression fits, red lines indicate LOA (+/- 1.96 SD) in Bland-Altman plots, and green lines indicate the mean difference between QCT-FE and DVC.

5.4.2 Reaction forces

Isotropic QCT-FE models were able to explain 75.6-79.4% of the variance in reaction force (Table 5-6). Normalized RMSE% between measured and FE predicted reaction forces ranged from 11.8% to 248% (Table 5-6). We obtained similar results for models using a uniform orthotropic model (constant anisotropy, orientation) for both trabecular and cortical bone (*not reported*). Incorporating spatially varying trabecular anisotropy via Cowin's fabric-elasticity equations offered similar results to those of Nazemi et al. (R^2:0.78; RMSE%:12.2-12.4%) (Table 5-7). For interpretation, linear regression plots and Bland-Altman plots are provided for the isotropic and anisotropic models offering the highest explained variance and lowest error, which includes the Nazemi et al approach, Keller & Snyder approach, and the Cowin & Rho approach (Figure 5-4). All other linear regression and Bland-Altman plots can be found in Appendix A. For all isotropic modeling approaches, the intercept did not differ from 0, whereas the slope differed from 1 for all approaches except for Keller & Rho, Keller & Snyder, Goulet & Snyder and Nazemi et al. For the models which used Cowin's fabric-elasticity equations, the slope and intercepts did not differ from 1 and 0, respectively. Bland-Altman plots indicated no mean bias for all models but many exhibited proportional bias (Appendix A). The models of Nazemi, Keller-Snyder and Cowin-Rho indicated no bias (Figure 5-4).

Table 5-6 Linear regression results comparing FE-predicted and experimentally measured reaction forces for the isotropic trabecular cortical models tested. Experimental reaction forces were taken as the relaxed load prior to HR-pQCT scanning. Slopes and intercepts differing from 1 and 0, respectively, are bold ($p < 0.05$).

Cortical model	**Trabecular model**	**Slope**	**Intercept [N]**	**R^2**	**RMSE%**
Rho et al.	Anderson et al.	**0.438**	74.8	0.767	60.2
	Goulet et al.	**0.759**	89.2	0.767	17.0
	Hodgskinson & Currey	**0.395**	52.5	0.770	74.5
	Keller	0.838	122	0.759	13.6
	Linde et al.	**0.323**	69.2	0.767	99.7
	Rho et al.	**0.169**	26.2	0.769	248
Snyder & Schneider	Anderson et al.	**0.471**	76.3	0.764	52.4
	Goulet et al.	0.810	90.2	0.763	14.7
	Hodgskinson & Currey	**0.425**	55.2	0.767	65.6
	Keller	0.894	121	0.756	13.2
	Linde et al.	**0.349**	71.1	0.764	88.5
	Rho et al.	**0.182**	32.0	0.764	226
Nazemi et al.	Nazemi et al.	0.995	19.8	0.794	11.8

Table 5-7 Linear regression results comparing FE-predicted and experimentally measured reaction forces for the anisotropic trabecular model of Cowin et al., paired with the uniformly orthotropic cortical models. Experimental reaction forces were taken as the relaxed load prior to HR-pQCT scanning. Slopes and intercepts differing from 1 and 0, respectively, are bold ($p < 0.05$).

Cortical model	**Trabecular model**	**Slope**	**Intercept [N]**	**R^2**	**RMSE%**
Rho et al.	Cowin et al.	0.942	76.1	0.783	12.2
Snyder & Schneider	Cowin et al.	0.938	80.8	0.780	12.4

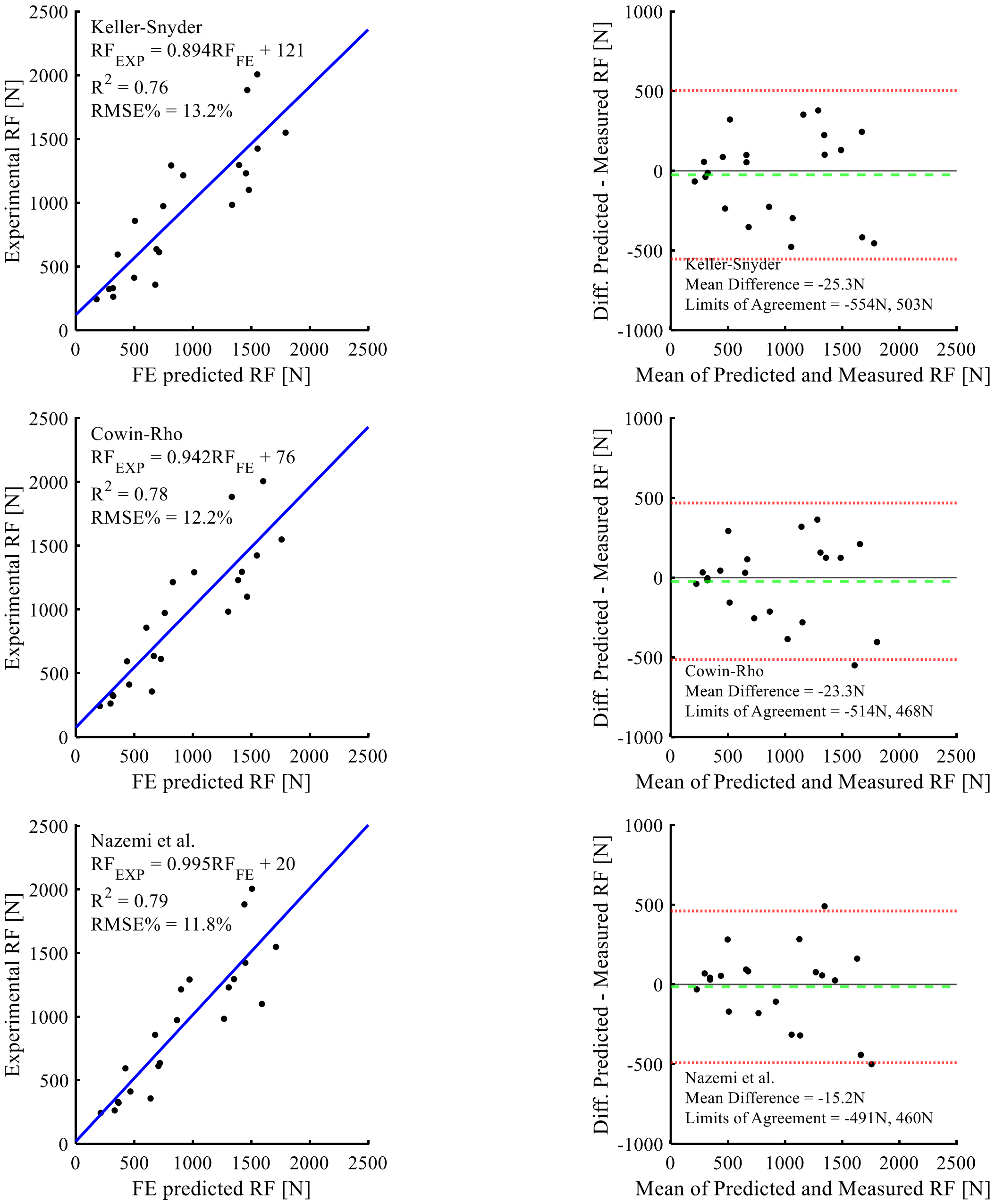

Figure 5-4 Linear regression and Bland-Altman plots comparing FE-predicted and experimentally measured reaction forces for the modelling approaches of Keller & Snyder, Cowin & Rho, and Nazemi et al. Blue lines are the least-squares fit regressions, red lines indicate LOA (+/- 1.96 SD) in Bland-Altman plots, and green lines indicate the mean difference between QCT-FE and DVC.

5.5 Discussion

The objective of this study was to apply different combinations of trabecular and cortical-specific relationships from the literature to QCT-FE models of the proximal tibia and identify those which resulted in highest explained variance and lowest error for internal displacement measurements and external reaction forces. Previous studies have evaluated the effects of different selected E-BMD relationships on model accuracy, but only for surface phenomena (strains, stiffness). This is the first study to compare FE-predicted and DVC-measured displacements in a long human bone, and the first to investigate the effects of different relationships on the accuracy of predictions of internal bone mechanics. Explained variance in DVC displacement measurements was >98% regardless of the combination of trabecular and cortical model. Explained variance in reaction force ranged from 0.76 to 0.79. Of the isotropic models tested, Nazemi et al.'s optimized trabecular and cortical E-BMD relationships (relative to the other isotropic models) resulted in lowest displacement RMSE% (4.03%), lowest reaction force RMSE% (11.8%) and highest explained variance in reaction forces (79%). Combining Cowin's fabric-elasticity equations for modeling trabecular bone's spatially varying anisotropy and the E-BMD relationship of Rho et al. for modeling uniformly orthotropic cortical bone resulted in the lowest overall displacement RMSE% (4.23%), low reaction force RMSE% (12.2%) and high explained variance in experimental reaction forces (78%).

Results from previous DVC-FE validation studies are similar to ours, reporting displacement RMSE% below 3% with R^2 greater than 0.97 for all components [23,109,110]. Regression slopes reported between FE-predicted and DVC measured displacements have historically been very close to 1 for all directions, with the exception of Zauel et al. who reported systematic under-predictions of displacements normal to the testing direction for µFE models of trabecular bone [21]. Although the RMSE% of all our displacement components was very low, the linear regression slopes and Bland-Altman plots indicated that our QCT-FE models under-predicted displacements in the medial-lateral (*x*) direction (slope >1.12). Incorporating spatially varying trabecular anisotropy did affect the accuracy of our models in the medial-lateral coordinate direction, specifically lowering RMSE%, yet this improvement was not reflected in the regression slope. Medial displacements in our experiments were primarily caused by bending of the tibia shaft due to the application of offset loads with respect to the specimens' neutral axes; therefore, one explanation for under-predicted medial displacements would be that models were overly stiff in bending. To rule out the role of element shear locking (and subsequent model stiffening), we also tested elements with reduced integration (with appropriate hourglass controls), though no improvements were found. Another possible explanation is that small under-estimations of axial displacements near the site of load application resulted in less bending, reducing the predicted planar displacements. Incorporating partial volume (PV) correction [62] may remedy this issue, thereby recovering the true stiffness of elements on the subchondral surface and encouraging the transfer of larger, local displacements through the rest of the specimen.

Our range of values for displacement RMSE% were narrow, with RMSE% for individual components ranging from 2.08% to 3.80% and overall RMSE% ranging from 3.87% to 4.38%. These small changes are consistent with observations from a previous study investigating the effect of selected E-BMD on agreement between FE predicted and experimentally measured strains of the distal radius, where RMSE% ranged from 13.2% to 14.2% depending on the selected E-BMD [17]. In our case, enforcing DVC-driven displacement BCs, rather than force BCs, imposed upper limits on the disagreement possible between experimental and FE displacements. The practice of using DVC-driven BCs is commonplace in DVC-based FE validation studies [21–23,92,110], as it is otherwise difficult to account for the subtle variations in contact force distributions on the loaded surfaces during experimental testing. When idealized force BCs are imposed instead, the predictive ability of the resulting FE models is very poor [23,92], making it impossible to capture some of the differences due to changes in modeling approaches, such as the selected E-BMD. Despite our narrow range for RMSE% obtained for different combinations of trabecular and cortical models, differences in accuracy were generally consistent across the different displacement components. Accounting for spatial variations of trabecular anisotropy using Cowin's fabric-elasticity equations led to a slight reduction in RMSE% for at least two of the three displacement components when compared to the other trabecular models tested.

Although displacement RMSE% were small, to get a complete picture of model agreement, however, it is necessary to also assess reaction force agreement between FE predicted and experimental findings. Here, reaction force predictions were far more variable than displacements, with a wider range of RMSE% for the different combinations of E-BMD (11.8% to 248%). This was expected since the power law E-BMD relationships tested have a large range of predicted values for a given density. By fixing displacements on the loaded surfaces with DVC-driven BCs, reaction forces were left unconstrained and scaled appropriately to ensure equilibrium. The wide range of RMSE% in our results for different E-BMD is similar to the range reported by Nazemi et al. for QCT-FE predictions of subchondral stiffness using displacement BCs (16.6% to 337.6%) [18]. Our results indicate a similar predictive ability for reaction forces (maximum R^2 of 0.79) when compared to the maximum of R^2 of 0.77 obtained by Nazemi et al in their subchondral surface stiffness study. One explanation for the remaining unexplained variance in reaction forces relates to the applied BCs. Manual segmentation of the contact surface between the composite indenter and the subchondral surface was non-trivial, with PV effects making it difficult to identify the boundaries of the indenter. Errors in identifying the appropriate nodes to apply boundary conditions will have resulted in under or over-predictions of reaction forces for a given specimen. Machining of the subchondral surface to ensure uniform contact with the indenter would have reduced these errors [22]; however, the decision to not do so was motivated by the desire to leave the subchondral bone unaltered. Accurate characterization of the subchondral bone is vital for investigating factors in OA progression, as it directly underlies the meniscus and articular cartilage. One potential solution in future experimental work would be to create composite indenters specific to each compartment's topology, ensuring uniform contact.

Similar to findings from other studies, our results indicate that for bone sites primarily comprised of trabecular tissue, relationships which predict a lower elastic modulus generally improve QCT-FE predictions [18,19,22]. Our displacement RMSE% and reaction force RMSE% were relatively insensitive to changes in the selected cortical model, but sensitive to the trabecular model. This is in line with previous observations that mechanical properties of the trabecular bone are the primary determinant of stiffness at the end-sites of long bones [26,33]. Even for models of the scapula, changes in the trabecular relationship resulted in more variability in reaction force predictions than changes to the cortical model [22]. Gibson et al. suggested that apparent compressive elastic modulus should exhibit a quadratic or cubic density dependence (power law with exponent of 2 or 3) [133], yet our results did not appear to exhibit any dependence on trabecular exponent. Our trabecular exponents ranged from 1.0 (Nazemi et al.) to 2.57 (Keller), with Nazemi et al., Keller, and Goulet et al. providing the lowest displacement and reaction force RMSE% of the isotropic models, despite very different exponents. Therefore, it appears that the mean mapped modulus of the relationships over the entire trabecular density range, rather than the power law exponent, are of primary importance for model accuracy at the proximal tibia.

This study has several strengths that require consideration. First, the accuracy of reaction forces and internal displacements were both assessed, allowing for comparisons between the two. Second, a total of 15 unique combinations of trabecular and cortical models were tested, providing a thorough test of the effect of mapped material properties on displacement and reaction force predictions. Third, the experimental testing performed in this study resulted in a large range of displacements in all coordinate directions compared to previous DVC-FE studies [23,109,110], providing a more robust test of the models compared to pure axial compression aligned with the neutral axes of specimens. Due to the offset loading condition tested here, shear and bending components were present. Fourth, homogenized models were used which did not directly model the trabecular microarchitecture. While these models are a simplification, they are more clinically relevant and less computationally expensive, making them a valuable tool once validated.

Limitations of this study pertain to the specimens themselves and assumptions/approximations made in their corresponding FE models. First, the cadaveric samples used were formalin-fixed (embalmed), rather than fresh-frozen. Some studies have reported reductions in elastic modulus after formalin fixation [134], while others have reported no changes in modulus or specimen stiffness [135,136]. The results of this study and the recommendations regarding choice of E-BMD match those of previous studies using fresh-frozen proximal tibiae [19,78], suggesting that any mechanical changes resulting from formalin fixation did not affect relative comparisons between different selected E-BMD. Secondly, our sample size of only 5 specimens from 4 donors was low; however, a larger sample sizes was not feasible, due to the time-consuming data collection involved in DVC studies (in this case, more than 180 hours per specimen, including dissection and potting, scanning and reconstruction, DVC, segmentation and FE model creation). Third, the QCT-FE models used here were voxel-based and did not accurately model the smooth curved surfaces of the tibia. This approach was chosen to further automate the meshing process, streamlining model creation. The use of a geometrically accurate mesh consisting of quadratic tetrahedral elements, rather than cubic elements, combined with a partial volume correction scheme, may further increase model accuracy. Fourth, our QCT-FE models were based on simulated QCT scans created by downsampling HR-pQCT and adding noise, which represents a best-case scenario compared to true QCT imaging and registration with HR-pQCT images. This decision was made to reduce the overall data collection efforts as well as eliminate errors due to registration of separate HR-pQCT and QCT scans. Fifth, the conclusions of this study are limited to the proximal tibia, and the loading regimes/conditions tested. Further studies are required to validate the internal strain/displacement predictions of other bones such as the patella or femur, and for other loading conditions, such as torsional loading and post-yield behaviour. As well, the optimal relationships identified here were initially developed for models of local, quasi-static compression, and have not been tested for other loading conditions or rates. In this study, we used the relaxed load prior to imaging for experimental validation [22,24,110]; this was used rather than peak load, as displacements from DVC were obtained for the same relaxed state, after stress-relaxation and slipping of the indenter on the bone surface had concluded. Our models are valid for static loading, though further validations should investigate the inclusion of bone's rate-dependent properties [137] to permit more physiologically relevant loading conditions.

5.6 Conclusion

This study validated QCT-FE predictions of internal bone displacements and external reaction forces in the proximal tibia using DVC, testing a total of 15 unique combinations of trabecular and cortical models. For isotropic models, Nazemi et al.'s optimized trabecular and cortical E-BMD relationships provided best agreement with experimental measurements for both internal bone displacements (RMSE%=4.03%, R^2>0.98) and reaction forces (RMSE%=11.8%, R^2=0.79). If modelling anisotropy, the combination of Cowin's fabric elasticity equations for trabecular bone and the E-BMD relationship of Rho et al. for cortical bone provided best agreement with experimental measurements for internal bone displacements (RMSE%=3.87%, R^2>0.98) and reaction forces (RMSE%=12.2%, R^2=0.78). Our results and conclusions regarding optimal trabecular and cortical models for the proximal tibia are in agreement with previous studies, suggesting that models valid for measures of local subchondral stiffness are also valid for internal bone mechanics.

CHAPTER 6

6 INTEGRATED DISCUSSION

6.1 Overview of findings

Subject-specific QCT-FE models of the proximal tibia have been previously validated by comparison of FE predictions to experimental measures of cortical strains, stiffness and failure load, with good agreement. However, the accuracy of predictions of internal bone mechanics such as displacement has not been tested. This research sought to address this gap, by first quantifying the measurement error associated with HR-pQCT based DVC, a means to measure 3D internal bone displacements in long bones, and then using this tool to measure experimental displacements in human proximal tibiae for comparison to FE predictions.

A key achievement of **Chapter 4** (Precision of Internal Displacement Measurements in Long Bones using HR-pQCT and DVC) was that we achieved sub-voxel displacement precision with DVC in large regions of interest (SD<0.17 voxels, LSC<0.46 voxels). Historically, DVC studies have been limited to smaller bone specimens, primarily due to size constraints within available scanning equipment and the difficulties associated with large-volume high-resolution scanning. By proposing modifications to the existing scanning protocol, which can be implemented with no additional operator intervention, we have made HR-pQCT a viable option for studying bone mechanics in large specimens. We also found that image denoising had little effect on displacement errors from HR-pQCT based DVC with the tested methods and parameters, and suggest that this step may not be necessary to obtain acceptable measurement precision.

A key achievement of **Chapter 5** (Experimental Validation of QCT-FE Models of the Proximal Tibia for Internal Displacements and External Reaction Forces using DVC: The Effect of Assigned Material Properties) was that we provided a thorough experimental validation of existing QCT-FE modeling methods for the proximal tibia, assessing the accuracy of internal displacement measurements as well as reaction forces. Our results corroborate the conclusions of existing studies, suggesting that models valid for measures of local subchondral stiffness are also valid for internal bone displacements. We also found that including spatially varying trabecular anisotropy modestly improved predictions of internal bone displacements compared to simpler isotropic models (as previously found by Nazemi et al [78]). The results of this study will inform future QCT-FE modeling studies regarding selection of material properties. As well, as the first study to investigate experimentally measured internal displacements in long human bones using DVC, this work will serve as a guide to future studies of long bones at other anatomical locations.

6.2 Contributions

This research makes several contributions to the field that should be mentioned:

i. This is the first study to thoroughly investigate the errors associated with HR-pQCT based DVC (inter-block displacements) and provide recommendations for their mitigation.
ii. This is the first study to investigate the agreement of QCT-FE predictions of internal bone displacements in the proximal tibia with experimental measures.

6.3 Clinical Significance

Our findings provide evidence that QCT-FE models of the proximal tibia can accurately predict internal bone displacements, with low error and high explained variance. This research suggests that QCT-FE can be trusted as a non-invasive tool for predicting internal bone mechanics. Potential applications of these validated models include investigating the role of bone in OA diagnostics, initiation and progression, studying the effects of clinical interventions such as drug therapy or exercise regimens on internal stress/strain distributions and predicted bone stiffness/failure load, and for pre-operative planning of total knee replacement surgeries to limit implant motion, stress-shielding and subsequent revisions.

6.4 Future work

i. The registration and stitching code used in Chapter 4 to create the full HR-pQCT image volumes used 3 DOF (translation) registration with linear interpolation. The addition of rotational DOFs, even a single one about the longitudinal scan axis (*z*-direction), may lead to improvements in registration, further reducing inter-block displacement errors. Similarly, increasing interpolation order to cubic or spline may improve registration quality. These additional computational loads may necessitate the use of graphics processing units (GPUs) to maintain reasonable processing times.

ii. HR-pQCT imaging was performed using a first-generation XtremeCT scanner. The newer, second generation of HR-pQCT (XtremeCT II) has a higher spatial resolution and slightly larger bore. It would be worthwhile performing zero-strain DVC analyses with the XtremeCT II to determine whether this tool improves displacement measurement error.

iii. Displacement predictions from QCT-FE were compared to experiment for only a single loading condition (offset axial compression). For a more thorough test of the recommended trabecular and cortical models, accuracy should also be assessed for torsional loading conditions.

iv. The boundary conditions in Chapter 5 were interpolated from DVC measurement points, giving a best-case scenario for the QCT-FE models. Generally, researchers and clinicians do not have access to this information and must make assumptions regarding the applied boundary conditions. Previous DVC-FE studies have compared predictions from models using idealized (assumed) BCs to those from models with DVC-driven BCs, concluding that idealized BCs cannot accurately replicate the experiment. More research is necessary in this area to guide researchers and clinicians by identifying general patterns of contact forces or displacements to apply to the medial and lateral plateaus that result in good agreement with experimental findings.

v. This study focused solely on the effect of bone's mechanical properties on model accuracy. Soft tissue (articular cartilage, meniscus) separates the bones in the knee joint, and its properties exhibit a large degree of loading rate dependence. For a valid model of the entire knee joint, additional studies are required to investigate the effects of assumed mechanical properties of the soft tissue in a variety of loading conditions. Furthermore, the optimal trabecular and cortical models for the tibia may not be optimal for modeling the femur, patella or fibula, as E-BMD relationships are known to depend on anatomical site.

REFERENCES

1. Zannoni C, Mantovani R, Viceconti M. Material properties assignment to finite element models of bone structures: A new method. Med Eng Phys. 1999;20(10):735–40.

2. Hunter DJ, Felson DT. Osteoarthritis. Br Med J. 2006;332:639–42.

3. Goldring SR. Role of Bone in Osteoarthritis Pathogenesis. Med Clin North Am. 2009;93(1):25–35.

4. Bombardier C, Hawker G, Mosher D. The Impact of Arthritis in Canada: Today and Over the Next 30 Years. Fall 2011. Ottawa: Arthritis Alliance of Canada; 2011.

5. McErlain DD, Milner JS, Ivanov TG, Jencikova-Celerin L, Pollmann SI, Holdsworth DW. Subchondral cysts create increased intra-osseous stress in early knee OA: A finite element analysis using simulated lesions. Bone. 2011;48(3):639–46.

6. Arjmand H, Nazemi M, Kontulainen SA, McLennan CE, Hunter DJ, Wilson DR, et al. Mechanical Metrics of the Proximal Tibia are Precise and Differentiate Osteoarthritic and Normal Knees: A Finite Element Study. Sci Rep. 2018;8(1):1–10.

7. Venäläinen MS, Mononen ME, Väänänen SP, Jurvelin JS, Töyräs J, Virén T, et al. Effect of bone inhomogeneity on tibiofemoral contact mechanics during physiological loading. J Biomech. 2016;49(7):1111–20.

8. Edwards WB, Schnitzer TJ, Troy KL. Torsional stiffness and strength of the proximal tibia are better predicted by finite element models than DXA or QCT. J Biomech. 2013;46(10):1655–62.

9. Keyak JH, Rossi SA, Jones KA, Skinner HB. Prediction of femoral fracture load using

automated finite element modeling. J Biomech. 1998;31(2):125–33.

10. Bougherara H, Zdero R, Mahboob Z, Dubov A, Shah S, Schemitsch EH. The biomechanics of a validated finite element model of stress shielding in a novel hybrid total knee replacement. Proc Inst Mech Eng Part H J Eng Med. 2010;224(10):1209–19.

11. Au AG, James Raso V, Liggins AB, Amirfazli A. Contribution of loading conditions and material properties to stress shielding near the tibial component of total knee replacements. J Biomech. 2007;40(6):1410–6.

12. Huiskes R, Weinans H, Van Rietbergen B. The relationship between stress shielding and bone resorption around total hip stems and the effects of flexible materials. Clin Orthop Relat Res. 1992;(274):124–34.

13. Helgason B, Perilli E, Schileo E, Taddei F, Brynjólfsson S, Viceconti M. Mathematical relationships between bone density and mechanical properties: A literature review. Clin Biomech. 2008;23(2):135–46.

14. Morgan EF, Bayraktar HH, Keaveny TM. Trabecular bone modulus-density relationships depend on anatomic site. J Biomech. 2003;36(7):897–904.

15. Taddei F, Schileo E, Helgason B, Cristofolini L, Viceconti M. The material mapping strategy influences the accuracy of CT-based finite element models of bones: An evaluation against experimental measurements. Med Eng Phys. 2007;29(9):973–9.

16. Austman RL, Milner JS, Holdsworth DW, Dunning CE. The effect of the density-modulus relationship selected to apply material properties in a finite element model of long bone. J Biomech. 2008;

17. Edwards WB, Troy KL. Finite element prediction of surface strain and fracture strength at the distal radius. Med Eng Phys. 2012;34(3):290–8.

18. Nazemi SM, Amini M, Kontulainen SA, Milner JS, Holdsworth DW, Masri BA, et al. Prediction of local proximal tibial subchondral bone structural stiffness using subject-specific finite element modeling: Effect of selected density-modulus relationship. Clin Biomech. 2015;30(7):703–12.

19. Nazemi SM, Amini M, Kontulainen SA, Milner JS, Holdsworth DW, Masri BA, et al. Optimizing finite element predictions of local subchondral bone structural stiffness using neural network-derived density-modulus relationships for proximal tibial subchondral cortical and trabecular bone. Clin Biomech. 2017;41:1–8.

20. Bay BK, Smith TS, Fyhrie DP, Saad M. Digital volume correlation: Three-dimensional strain mapping using x-ray tomography. Exp Mech. 1999;39(3):217–26.

21. Zauel R, Yeni YN, Bay BK, Dong XN, Fyhrie DP. Comparison of the linear finite element prediction of deformation and strain of human cancellous bone to 3D digital volume correlation measurements. J Biomech Eng. 2006;128(1):1–6.

22. Knowles NK, Kusins J, Faieghi M, Ryan M, Dall'Ara E, Ferreira LM. Material Mapping of QCT-Derived Scapular Models: A Comparison with Micro-CT Loaded Specimens Using Digital Volume Correlation. Ann Biomed Eng. 2019;47(11):2188–98.

23. Chen Y, Dall'Ara E, Sales E, Manda K, Wallace R, Pankaj P, et al. Micro-CT based finite element models of cancellous bone predict accurately displacement once the boundary condition is well replicated: A validation study. J Mech Behav Biomed Mater. 2017;65(Janaury):644–51.

24. Basler SE, Mueller TL, Christen D, Wirth AJ, Müller R, van Lenthe GH. Towards validation of computational analyses of peri-implant displacements by means of experimentally obtained displacement maps. Comput Methods Biomech Biomed Engin. 2011;14(2):165–74.

25. Rapagna S, Berahmani S, Wyers CE, van den Bergh JPW, Reynolds KJ, Tozzi G, et al. Quantification of human bone microarchitecture damage in press-fit femoral knee implantation using HR-pQCT and digital volume correlation. J Mech Behav Biomed Mater. 2019;97(May):278–87.

26. Amini M, Nazemi SM, Lanovaz JL, Kontulainen S, Masri BA, Wilson DR, et al. Individual and combined effects of OA-related subchondral bone alterations on proximal tibial surface stiffness: A parametric finite element modeling study. Med Eng Phys. 2015;37(8):783–91.

27. Martini F, Timmons M, Tallitsch R. Human Anatomy. 7th ed. San Francisco: Benjamin Cummings; 2012.

28. Buckwalter JA, Mankin HJ, Grodzinsky AJ. Articular cartilage and osteoarthritis. Instructional course lectures. 2005.

29. Venäläinen MS, Mononen ME, Jurvelin JS, Töyräs J, Virén T, Korhonen RK. Importance of Material Properties and Porosity of Bone on Mechanical Response of Articular Cartilage in Human Knee Joint - A Two-Dimensional Finite Element Study. J Biomech Eng. 2014;136(12):1–8.

30. Brown TD, Radin EL, Martin RB, Burr DB. Finite element studies of some juxtarticular stress changes due to localized subchondral stiffening. J Biomech. 1984;

31. Gray H. Gray's Anatomy. 20th ed. Lewis WH, editor. Philadelphia: Lea & Febiger; 1918. 1396 p.

32. Keaveny TM, Morgan EF, Niebur GL, Yeh OC. Biomechanics of Trabecular Bone. Annu Rev Biomed Eng. 2001;3(1):307–33.

33. Chang G, Rajapakse CS, Babb JS, Honig SP, Recht MP, Regatte RR. In vivo estimation of bone stiffness at the distal femur and proximal tibia using ultra-high-field 7-Tesla magnetic resonance imaging and micro-finite element analysis. J Bone Miner Metab. 2012;30(2):243–51.

34. Radin EL, Paul IL. Does cartilage compliance reduce skeletal impact loads?. the relative force-attenuating properties of articular cartilage, synovial fluid, periarticular soft tissues and bone. Arthritis Rheum. 1970;13(2):139–44.

35. Ding M, Dalstra M, Linde F, Hvid I. Changes in the stiffness of the human tibial cartilage-bone complex in early-stage osteoarthrosis. Acta Orthop Scand. 1998;69(4):358–62.

36. Li B, Aspden RM. Composition and mechanical properties of cancellous bone from the femoral head of patients with osteoporosis or osteoarthritis. J Bone Miner Res. 1997;12(4):641–51.

37. Day JS, Ding M, Van Der Linden JC, Hvid I, Sumner DR, Weinans H. A decreased subchondral trabecular bone tissue elastic modulus is associated with pre-arthritic cartilage damage. J Orthop Res. 2001;19(5):914–8.

38. Boschetti F, Peretti GM. Tensile and compressive properties of healthy and osteoarthritic human articular cartilage. In: Biorheology. 2008. p. 337–44.

39. Obeid EMH, Adams MA, Newman JH. Mechanical properties of articular cartilage in knees with unicompartmental osteoarthritis. J Bone Jt Surg - Ser B. 1994;76(2):315–9.

40. Felson DT. Osteoarthritis of the knee. N Engl J Med. 2006;354(8):841–8.

41. Ridzwan MIZ, Shuib S, Hassan AY, Shokri AA, Mohammad Ibrahim MN. Problem of stress shielding and improvement to the hip implant designs: A review. J Med Sci. 2007;7(3):460–7.

42. Engh C, Bobyn J. Porous-coated hip replacement. J Bone Jt Surg. 1987;69(1):45–55.

43. Nagels J, Stokdijk M, Rozing PM. Stress shielding and bone resorption in shoulder arthroplasty. J Shoulder Elb Surg. 2003;12(1):35–9.

44. Wolff J. The Law of Bone Remodelling. Heidelberg, Berlin: Springer Berlin Heidelberg; 1986.

45. Venäläinen MS, Mononen ME, Salo J, Räsänen LP, Jurvelin JS, Töyräs J, et al. Quantitative Evaluation of the Mechanical Risks Caused by Focal Cartilage Defects in the Knee. Sci Rep. 2016;6(October):1–11.

46. Liukkonen MK, Mononen ME, Klets O, Arokoski JP, Saarakkala S, Korhonen RK. Simulation of subject-specific progression of knee osteoarthritis and comparison to experimental follow-up data: Data from the osteoarthritis initiative. Sci Rep. 2017;7(1):1–14.

47. Klets O, Mononen ME, Liukkonen MK, Nevalainen MT, Nieminen MT, Saarakkala S, et al. Estimation of the Effect of Body Weight on the Development of Osteoarthritis Based on Cumulative Stresses in Cartilage: Data from the Osteoarthritis Initiative. Ann Biomed Eng.

2018;46(2):334–44.

48. Stoer J, Bulirsch R. Introduction to Numerical Analysis. New York: Springer; 2002.

49. Irons BM. A frontal solution program for finite element analysis. Int J Numer Methods Eng. 1970;2:5–32.

50. Duff IS, Reid JK. The Multifrontal Solution of Indefinite Sparse Symmetric Linear. ACM Trans Math Softw. 1983;9(3):302–25.

51. Shewchuk J. An Introduction to the Conjugate Gradient Method Without the Agonizing Pain. Association for Computing Machinery. Pittsburgh; 1994.

52. Niebur GL, Feldstein MJ, Yuen JC, Chen TJ, Keaveny TM. High-resolution finite element models with tissue strength asymmetry accurately predict failure of trabecular bone. J Biomech. 2000;33(12):1575–83.

53. Van Rietbergen B, Weinans H, Huiskes R, Polman BJW. Computational strategies for iterative solutions of large fem applications employing voxel data. Int J Numer Methods Eng. 1996;39(16):2743–67.

54. Barrett R, Berry M, Chan TF, Demmel J, Donato J, Dongarra J, et al. Templates for the Solution of Linear Systems: Building Blocks for Iterative Methods. Society for Industrial and Applied Mathematics. Philadelphia; 1994.

55. Hayes WC, Swenson LW, Schurman DJ. Axisymmetric finite element analysis of the lateral tibial plateau. J Biomech. 1978;11(1–2):21–33.

56. Reggiani B, Cristofolini L, Varini E, Viceconti M. Predicting the subject-specific primary stability of cementless implants during pre-operative planning: Preliminary validation of

subject-specific finite-element models. J Biomech. 2007;40(11):2552–8.

57. Van Rietbergen B, Odgaard A, Kabel J, Huiskes R. Direct mechanics assessment of elastic symmetries and properties of trabecular bone architecture. J Biomech. 1996;29(12):1653–7.

58. Dall'Ara E, Luisier B, Schmidt R, Kainberger F, Zysset P, Pahr D. A nonlinear QCT-based finite element model validation study for the human femur tested in two configurations in vitro. Bone. 2013;52(1):27–38.

59. Keyak JH, Skinner HB. Three-dimensional finite element modelling of bone: effects of element size. J Biomed Eng. 1992;14(6):483–9.

60. Viceconti M, Bellingeri L, Cristofolini L, Toni A. A comparative study on different methods of automatic mesh generation of human femurs. Med Eng Phys. 1998;20(1):1–10.

61. Lorensen WE, Cline HE. Marching cubes: A high resolution 3D surface construction algorithm. In: Proceedings of the 14th Annual Conference on Computer Graphics and Interactive Techniques, SIGGRAPH 1987. 1987.

62. Helgason B, Taddei F, Pálsson H, Schileo E, Cristofolini L, Viceconti M, et al. A modified method for assigning material properties to FE models of bones. Med Eng Phys. 2008;30(4):444–53.

63. Gray HA, Taddei F, Zavatsky AB, Cristofolini L, Gill HS. Experimental validation of a finite element model of a human cadaveric tibia. J Biomech Eng. 2008;130(3):1–9.

64. Burkhart TA, Andrews DM, Dunning CE. Finite element modeling mesh quality, energy balance and validation methods: A review with recommendations associated with the

modeling of bone tissue. J Biomech. 2013;46(9):1477–88.

65. Knowles NK, Reeves JM, Ferreira LM. Quantitative Computed Tomography (QCT) derived Bone Mineral Density (BMD) in finite element studies: a review of the literature. J Exp Orthop. 2016;3(1):36.

66. Goulet RW, Goldstein SA, Ciarelli MJ, Kuhn JL, Brown MB, Feldkamp LA. The relationship between the structural and orthogonal compressive properties of trabecular bone. J Biomech. 1994;27(4):375–89.

67. Keller TS. Predicting the compressive mechanical behavior of bone. J Biomech. 1994;27(9):1159–68.

68. Rho JY, Ashman RB, Turner CH. Young's modulus of trabecular and cortical bone material: Ultrasonic and microtensile measurements. J Biomech. 1993;26(2):111–9.

69. Rho JY, Hobatho MC, Ashman RB. Relations of mechanical properties to density and CT numbers in human bone. Med Eng Phys. 1995;17(5):347–55.

70. Rho JY. An ultrasonic method for measuring the elastic properties of human tibial cortical and cancellous bone. Ultrasonics. 1996;34(8):777–83.

71. Anderson MJ, Keyak JH, Skinner HB. Compressive mechanical properties of human cancellous bone after gamma irradiation. J Bone Jt Surg - Ser A. 1992;74(5):747–52.

72. Ulrich D, Van Rietbergen B, Laib A, R̈uegsegger P. The ability of three-dimensional structural indices to reflect mechanical aspects of trabecular bone. Bone. 1999;25(1):55–60.

73. Enns-bray WS, Ariza O, Gilchrist S, Soyka RPW, Vogt PJ. Morphology based anisotropic finite element models of the proximal femur validated with experimental data.

2016;38:1339–47.

74. Turner CH, Cowin SC, Rho JY, Ashman RB, Rice JC. The fabric dependence of the orthotropic elastic constants of cancellous bone. J Biomech. 1990;

75. Kersh ME, Zysset PK, Pahr DH, Wolfram U, Larsson D, Pandy MG. Measurement of structural anisotropy in femoral trabecular bone using clinical-resolution CT images. J Biomech. 2013;46(15):2659–66.

76. Nazemi SM, Cooper DML, Johnston JD. Quantifying trabecular bone material anisotropy and orientation using low resolution clinical CT images: A feasibility study. Med Eng Phys. 2016;38(9):978–87.

77. Cowin SC. The relationship between the elasticity tensor and the fabric tensor. Mech Mater. 1985;4(2):137–47.

78. Nazemi SM, Kalajahi SMH, Cooper DML, Kontulainen SA, Holdsworth DW, Masri BA, et al. Accounting for spatial variation of trabecular anisotropy with subject-specific finite element modeling moderately improves predictions of local subchondral bone stiffness at the proximal tibia. J Biomech. 2017;59:101–8.

79. Taddei F, Pancanti A, Viceconti M. An improved method for the automatic mapping of computed tomography numbers onto finite element models. Med Eng Phys. 2004;26(1):61–9.

80. Chen G, Wu FY, Liu ZC, Yang K, Cui F. Comparisons of node-based and element-based approaches of assigning bone material properties onto subject-specific finite element models. Med Eng Phys. 2015;37(8):808–12.

81. Chen G, Schmutz B, Epari D, Rathnayaka K, Ibrahim S, Schuetz MA, et al. A new approach for assigning bone material properties from CT images into finite element models. J Biomech. 2010;43(5):1011–5.

82. Schileo E, Taddei F, Malandrino A, Cristofolini L, Viceconti M. Subject-specific finite element models can accurately predict strain levels in long bones. J Biomech. 2007;40(13):2982–9.

83. Austman RL, Milner JS, Holdsworth DW, Dunning CE. The effect of the density-modulus relationship selected to apply material properties in a finite element model of long bone. J Biomech. 2008;41(15):3171–6.

84. Burnett WD. Relationships between image-based and mechanical bone properties with pain in knee osteoarthritis. University of Saskatchewan; 2018.

85. Sztefek P, Vanleene M, Olsson R, Collinson R, Pitsillides AA, Shefelbine S. Using digital image correlation to determine bone surface strains during loading and after adaptation of the mouse tibia. J Biomech. 2010;43(4):599–605.

86. Väänänen SP, Amin Yavari S, Weinans H, Zadpoor AA, Jurvelin JS, Isaksson H. Repeatability of digital image correlation for measurement of surface strains in composite long bones. J Biomech. 2013;46(11):1928–32.

87. Gustafson H, Siegmund G, Cripton P. Comparison of Strain Rosettes and Digital Image Correlation for Measuring Vertebral Body Strain. J Biomech Eng. 2016;138(5).

88. Hussein AI, Barbone PE, Morgan EF. Digital volume correlation for study of the mechanics of whole bones. Procedia IUTAM. 2012;4:116–25.

89. Tozzi G, Zhang QH, Tong J. Microdamage assessment of bone-cement interfaces under monotonic and cyclic compression. J Biomech. 2014;47(14):3466–74.

90. Gillard F, Boardman R, Mavrogordato M, Hollis D, Sinclair I, Pierron F, et al. The application of digital volume correlation (DVC) to study the microstructural behaviour of trabecular bone during compression. J Mech Behav Biomed Mater. 2014;29:480–99.

91. Sukjamsri C, Geraldes DM, Gregory T, Ahmed F, Hollis D, Schenk S, et al. Digital volume correlation and micro-CT: An in-vitro technique for measuring full-field interface micromotion around polyethylene implants. J Biomech. 2015;48(12):3447–54.

92. Jackman TM, DelMonaco AM, Morgan EF. Accuracy of finite element analyses of CT scans in predictions of vertebral failure patterns under axial compression and anterior flexion. J Biomech. 2016;49(2):267–75.

93. Tozzi G, Danesi V, Palanca M, Cristofolini L. Elastic Full-Field Strain Analysis and Microdamage Progression in the Vertebral Body from Digital Volume Correlation. Strain. 2016;52(5):446–55.

94. Palanca M, Bodey AJ, Giorgi M, Viceconti M, Lacroix D, Cristofolini L, et al. Local displacement and strain uncertainties in different bone types by digital volume correlation of synchrotron microtomograms. J Biomech. 2017;58:27–36.

95. Christen D, Levchuk A, Schori S, Schneider P, Boyd SK, Müller R. Deformable image registration and 3D strain mapping for the quantitative assessment of cortical bone microdamage. J Mech Behav Biomed Mater. 2012;8:184–93.

96. Peña Fernández M, Barber AH, Blunn GW, Tozzi G. Optimization of digital volume

correlation computation in SR-microCT images of trabecular bone and bone-biomaterial systems. J Microsc. 2018;272(3):213–28.

97. LaVision. DaVis 10.0 Digital Volume Correlation Product Manual. Göttingen, Germany: LaVision GmbH; 2017. 2017 p.

98. Smith TS, Bay BK, Rashid MM. Digital volume correlation including rotational degrees of freedom during minimization. Exp Mech. 2002;42:272–8.

99. Roux S, Hild F, Viot P, Bernard D. Three-dimensional image correlation from X-ray computed tomography of solid foam. Compos Part A Appl Sci Manuf. 2008;39(8):1253–65.

100. Benoit A, Guérard S, Gillet B, Guillot G, Hild F, Mitton D, et al. 3D analysis from micro-MRI during in situ compression on cancellous bone. J Biomech. 2009;42(14):2381–6.

101. Palanca M, Tozzi G, Cristofolini L, Viceconti M, Dall'Ara E. Three-dimensional local measurements of bone strain and displacement: Comparison of three digital volume correlation approaches. J Biomech Eng. 2015;137(7):1–14.

102. Comini F, Palanca M, Cristofolini L, Dall'Ara E. Uncertainties of synchrotron microCT-based digital volume correlation bone strain measurements under simulated deformation. J Biomech. 2019;86:232–7.

103. Liu L, Morgan EF. Accuracy and precision of digital volume correlation in quantifying displacements and strains in trabecular bone. J Biomech. 2007;40(15):3516–20.

104. Dall'Ara E, Barber D, Viceconti M. About the inevitable compromise between spatial resolution and accuracy of strain measurement for bone tissue: A 3D zero-strain study. J

Biomech. 2014;47(12):2956–63.

105. Kroker A, Zhu Y, Manske SL, Barber R, Mohtadi N, Boyd SK. Quantitative in vivo assessment of bone microarchitecture in the human knee using HR-pQCT. Bone. 2017;97:43–8.

106. Gilchrist SM. Comparison of proximal femur deformations, failures and fractures in quasi-static and inertially-driven simulations of a sideways fall from standing. University of British Colombia; 2014.

107. Buades A, Coll B, Morel JM. A non-local algorithm for image denoising. In: Proceedings - 2005 IEEE Computer Society Conference on Computer Vision and Pattern Recognition, CVPR 2005. 2005.

108. Chambolle A. An Algorithm for Total Variation Minimization and Applications. In: Journal of Mathematical Imaging and Vision. 2004.

109. Costa MC, Tozzi G, Cristofolini L, Danesi V, Viceconti M, Dall'Ara E. Micro finite element models of the vertebral body: Validation of local displacement predictions. PLoS One. 2017;12(7):1–18.

110. Kusins J, Knowles N, Ryan M, Dall'Ara E, Ferreira L. Performance of QCT-Derived scapula finite element models in predicting local displacements using digital volume correlation. J Mech Behav Biomed Mater. 2019;97(May):339–45.

111. Tozzi G, Dall'Ara E, Palanca M, Curto M, Innocente F, Cristofolini L. Strain uncertainties from two digital volume correlation approaches in prophylactically augmented vertebrae: Local analysis on bone and cement-bone microstructures. J Mech Behav Biomed Mater.

2017;67(December 2016):117–26.

112. Oliviero S, Giorgi M, Dall’Ara E. Validation of finite element models of the mouse tibia using digital volume correlation. J Mech Behav Biomed Mater. 2018;86(June):172–84.

113. Scanco Medical AG. XtremeCT User’s Guide. Revision 6. Brüttisellen, Switzerland; 2013.

114. Boas FE, Fleischmann D. CT artifacts: Causes and reduction techniques. Imaging Med. 2012;4(2):229–40.

115. Münch B, Trtik P, Marone F, Stampanoni M. Stripe and ring artifact removal with combined wavelet-Fourier filtering. EMPA Act. 2009;17(2009-2010 EMPA ACTIVITIES):34–5.

116. Nelder JA, Mead R. A Simplex Method for Function Minimization. Comput J. 1965;7(4):308–13.

117. Laib A, Hauselmann HJ, Ruegsegger P. In vivo high resolution 3D-QCT of the human forearm. Technol Heal Care. 1998;6(5–6):329–37.

118. Bonnick S Lou, Johnston CC, Kleerekoper M, Lindsay R, Miller P, Sherwood L, et al. Importance of precision in bone density measurements. J Clin Densitom. 2001;4(2):105–10.

119. Rapagna S, Berahmani S, Wyers CE, van den Bergh JPW, Reynolds KJ, Tozzi G, et al. Quantification of human bone microarchitecture damage in press-fit femoral knee implantation using HR-pQCT and digital volume correlation. J Mech Behav Biomed Mater. 2019;97(September 2019):278–87.

120. Peña Fernández M, Cipiccia S, Dall’Ara E, Bodey AJ, Parwani R, Pani M, et al. Effect of SR-microCT radiation on the mechanical integrity of trabecular bone using in situ

mechanical testing and digital volume correlation. J Mech Behav Biomed Mater. 2018;88(July):109–19.

121. Scanco Medical AG. XtremeCT II User's Guide. Revision 2. Brüttisellen, Switzerland; 2018.

122. Nazarian A, Müller R. Time-lapsed microstructural imaging of bone failure behavior. J Biomech. 2004;37(1):55–65.

123. Nagaraja S, Couse TL, Guldberg RE. Trabecular bone microdamage and microstructural stresses under uniaxial compression. J Biomech. 2005;38(4):707–16.

124. Westerweel J, Scarano F. Universal outlier detection for PIV data. Exp Fluids. 2005;39(6):1096–100.

125. Joemai RMS. Technical advances in multi-slice computed tomograpy: dose assessment and clinical optimizations. Leiden University; 2012.

126. Hodgskinson R, Currey JD. Young's modulus, density and material properties in cancellous bone over a large density range. J Mater Sci Mater Med. 1992;3:377–81.

127. Linde F, Hvid I, Madsen F. The effect of specimen geometry on the mechanical behavior of trabecular bone specimens. J Biomech. 1992;185(4):129–32.

128. Snyder SM, Schneider E. Estimation of mechanical properties of cortical bone by computed tomography. J Orthop Res. 1991;9(3):422–31.

129. Keyak JH, Lee IY, Skinner HB. Correlations between orthogonal mechanical properties and density of trabecular bone: use of different densitometric measures. J Biomed Mater Res. 1994;28(11):1329–36.

130. Keyak JH, Kaneko TS, Tehranzadeh J, Skinner HB. Predicting proximal femoral strength using structural engineering models. Clin Orthop Relat Res. 2005;437:219–28.

131. Carter DR, Hayes WC. The compressive behavior of bone as a two-phase porous structure. J Bone Jt Surg - Ser A. 1977;59(7):954–62.

132. Majcher K. Mechanical metrics of the proximal femur are precise and associated with hip muscle properties: a magnetic resonance based finite element study. University of Saskatchewan; 2020.

133. Gibson LJ. The mechanical behaviour of cancellous bone. J Biomech. 1985;18(5):317–28.

134. Öhman C, Dall'Ara E, Baleani M, Jan SVS, Viceconti M. The effects of embalming using a 4% formalin solution on the compressive mechanical properties of human cortical bone. Clin Biomech. 2008;23(10):1294–8.

135. Topp T, Müller T, Huss S, Kann PH, Weihe E, Ruchholtz S, et al. Embalmed and fresh frozen human bones in orthopedic cadaveric studies: Which bone is authentic and feasible? Acta Orthop. 2012;83(5):543–7.

136. Stefan U, Michael B, Werner S. Effects of three different preservation methods on the mechanical properties of human and bovine cortical bone. Bone. 2010;47(6):1048–53.

137. Linde F, Nørgaard P, Hvid I, Odgaard A, Søballe K. Mechanical properties of trabecular bone. Dependency on strain rate. J Biomech. 1991;24(9):803–9.

APPENDIX: REACTION FORCE FIGURES

For completeness, the reaction force figures (linear regression, Bland-Altman) which were not shown in Chapter 5 are presented here. Figure A-1 contains the linear regression and Bland-Altman plots for the pairing of the cortical model of Rho et al. with the trabecular models of Anderson et al., Goulet et al., Hodgskinson and Currey, Keller, Linde et al. and Rho et al. Figure A-2 contains the associated plots for the pairing of the cortical model of Snyder and Schneider with the trabecular models of Anderson et al., Cowin et al., Goulet et al., Hodgskinson and Currey, Linde et al. and Rho et al.

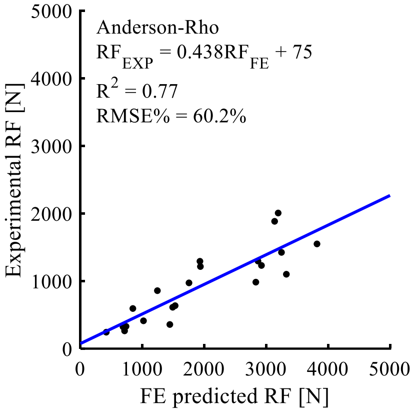
Anderson-Rho
$RF_{EXP} = 0.438RF_{FE} + 75$
$R^2 = 0.77$
RMSE% = 60.2%
Experimental RF [N]
FE predicted RF [N]
0
1000
2000
3000
4000
5000

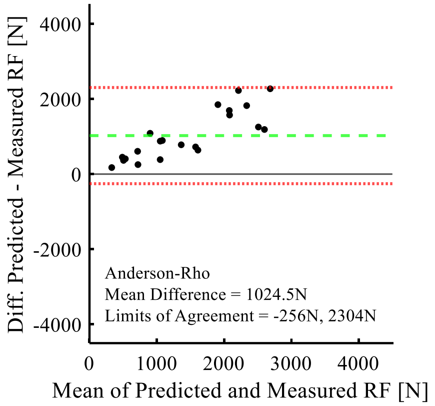
Anderson-Rho
Mean Difference = 1024.5N
Limits of Agreement = -256N, 2304N
Diff. Predicted - Measured RF [N]
Mean of Predicted and Measured RF [N]
4000
2000
0
-2000
-4000
0
1000
2000
3000
4000

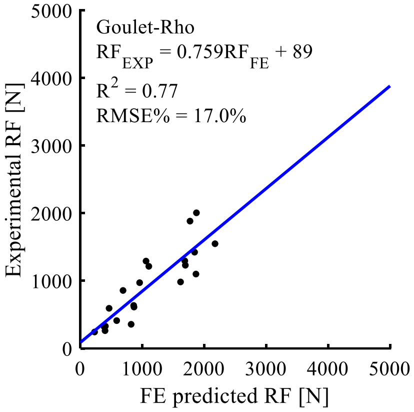
Goulet-Rho
$RF_{EXP} = 0.759RF_{FE} + 89$
$R^2 = 0.77$
RMSE% = 17.0%
Experimental RF [N]
FE predicted RF [N]
0
1000
2000
3000
4000
5000

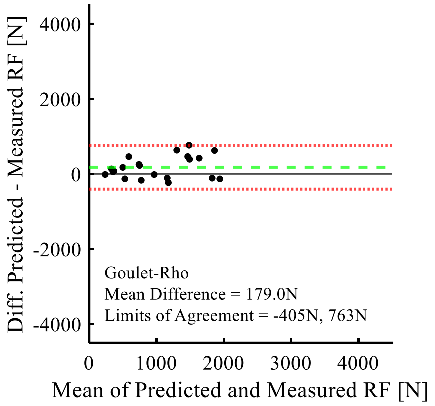
Goulet-Rho
Mean Difference = 179.0N
Limits of Agreement = -405N, 763N
Diff. Predicted - Measured RF [N]
Mean of Predicted and Measured RF [N]
4000
2000
0
-2000
-4000
0
1000
2000
3000
4000

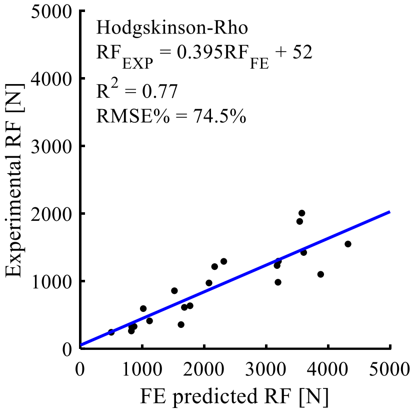
Hodgskinson-Rho
$RF_{EXP} = 0.395RF_{FE} + 52$
$R^2 = 0.77$
RMSE% = 74.5%
Experimental RF [N]
FE predicted RF [N]
0
1000
2000
3000
4000
5000

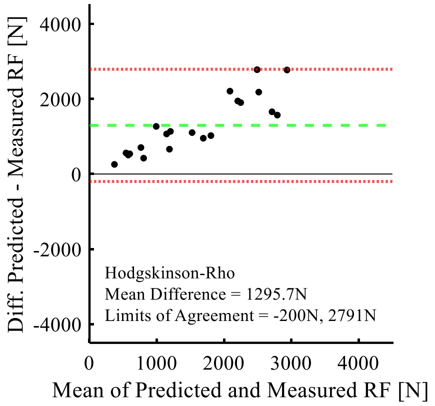
Hodgskinson-Rho
Mean Difference = 1295.7N
Limits of Agreement = -200N, 2791N
Diff. Predicted - Measured RF [N]
Mean of Predicted and Measured RF [N]
4000
2000
0
-2000
-4000
0
1000
2000
3000
4000

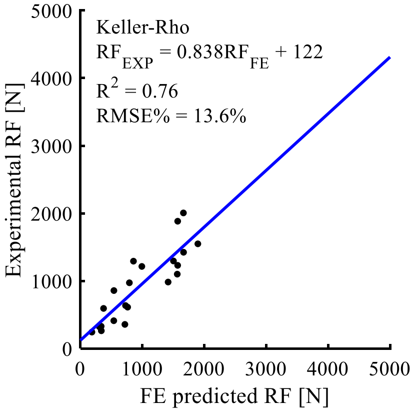
Keller-Rho
$RF_{EXP} = 0.838RF_{FE} + 122$
$R^2 = 0.76$
RMSE% = 13.6%
Experimental RF [N]
FE predicted RF [N]
0
1000
2000
3000
4000
5000

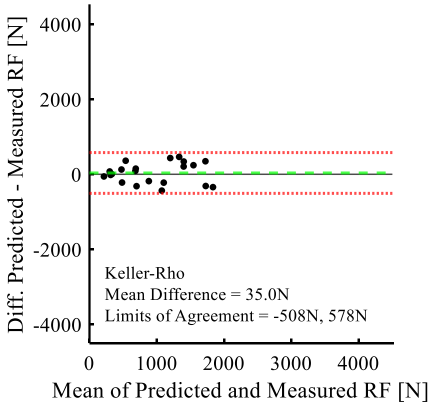
Keller-Rho
Mean Difference = 35.0N
Limits of Agreement = -508N, 578N
Diff. Predicted - Measured RF [N]
Mean of Predicted and Measured RF [N]
4000
2000
0
-2000
-4000
0
1000
2000
3000
4000

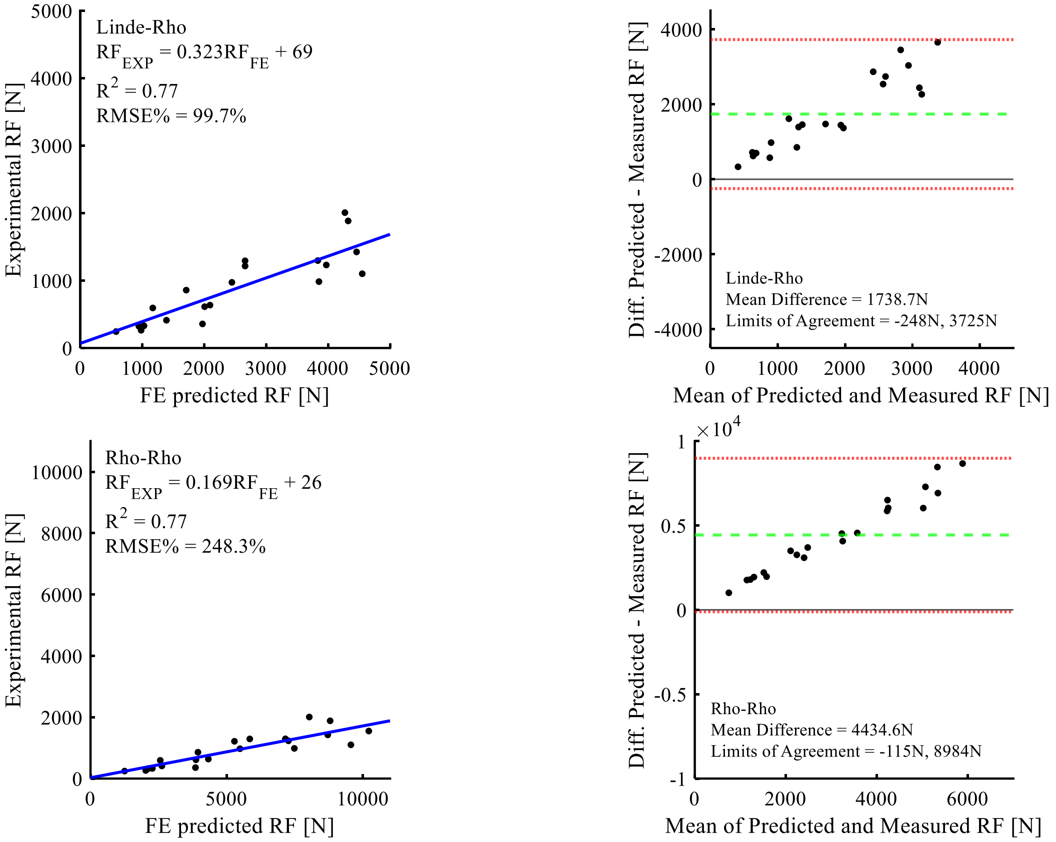

Figure A-1 Linear regression and Bland-Altman plots omitted from Chapter 5, for the various trabecular models combined with the cortical model of Rho et al. Blue lines are the least-squares fit regressions, red lines indicate LOA (+/- 1.96 SD) for Bland-Altman plots, and green lines indicate the mean difference between QCT-FE and DVC. Note the different scales for the trabecular relationship of Rho et al.

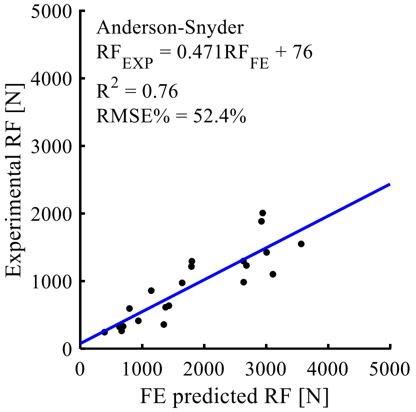
Anderson-Snyder
RF$_{EXP}$ = 0.471RF$_{FE}$ + 76
R^2 = 0.76
RMSE% = 52.4%
Experimental RF [N]
FE predicted RF [N]
0
1000
2000
3000
4000
5000

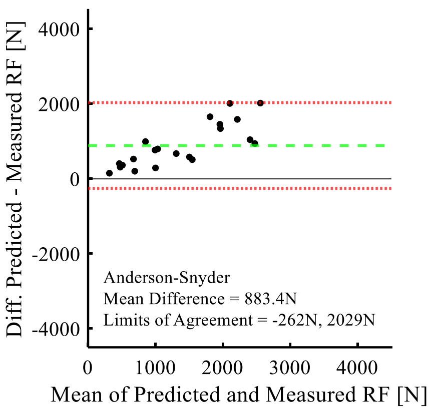
Anderson-Snyder
Mean Difference = 883.4N
Limits of Agreement = -262N, 2029N
Diff. Predicted - Measured RF [N]
Mean of Predicted and Measured RF [N]
4000
2000
0
-2000
-4000
0
1000
2000
3000
4000

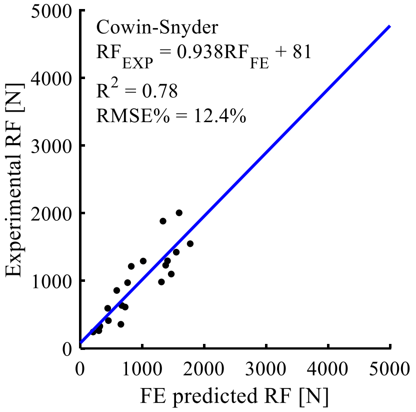
Cowin-Snyder
RF$_{EXP}$ = 0.938RF$_{FE}$ + 81
R^2 = 0.78
RMSE% = 12.4%
Experimental RF [N]
FE predicted RF [N]
0
1000
2000
3000
4000
5000

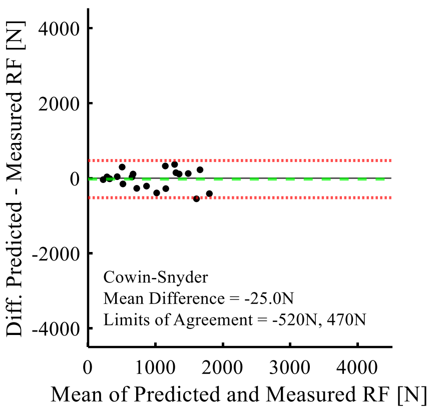
Cowin-Snyder
Mean Difference = -25.0N
Limits of Agreement = -520N, 470N
Diff. Predicted - Measured RF [N]
Mean of Predicted and Measured RF [N]
4000
2000
0
-2000
-4000
0
1000
2000
3000
4000

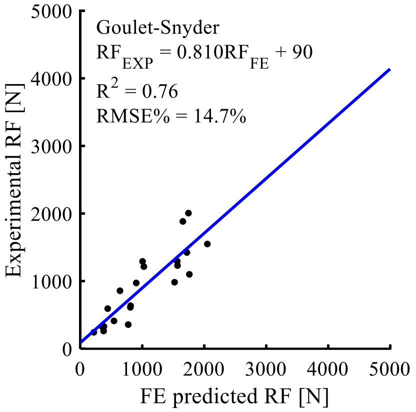
Goulet-Snyder
RF$_{EXP}$ = 0.810RF$_{FE}$ + 90
R^2 = 0.76
RMSE% = 14.7%
Experimental RF [N]
FE predicted RF [N]
0
1000
2000
3000
4000
5000

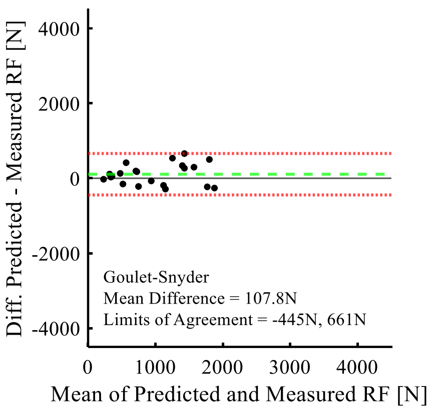
Goulet-Snyder
Mean Difference = 107.8N
Limits of Agreement = -445N, 661N
Diff. Predicted - Measured RF [N]
Mean of Predicted and Measured RF [N]
4000
2000
0
-2000
-4000
0
1000
2000
3000
4000

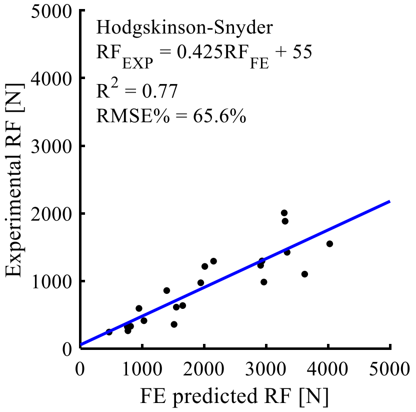
Hodgskinson-Snyder
RF$_{EXP}$ = 0.425RF$_{FE}$ + 55
R^2 = 0.77
RMSE% = 65.6%
Experimental RF [N]
FE predicted RF [N]
0
1000
2000
3000
4000
5000

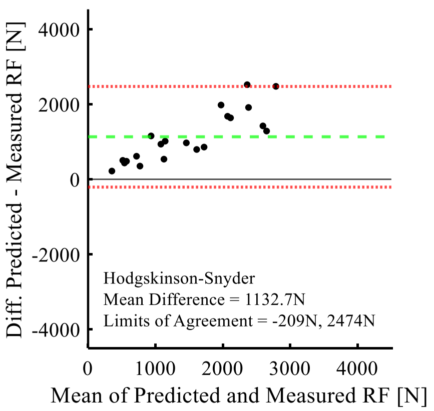
Hodgskinson-Snyder
Mean Difference = 1132.7N
Limits of Agreement = -209N, 2474N
Diff. Predicted - Measured RF [N]
Mean of Predicted and Measured RF [N]
4000
2000
0
-2000
-4000
0
1000
2000
3000
4000

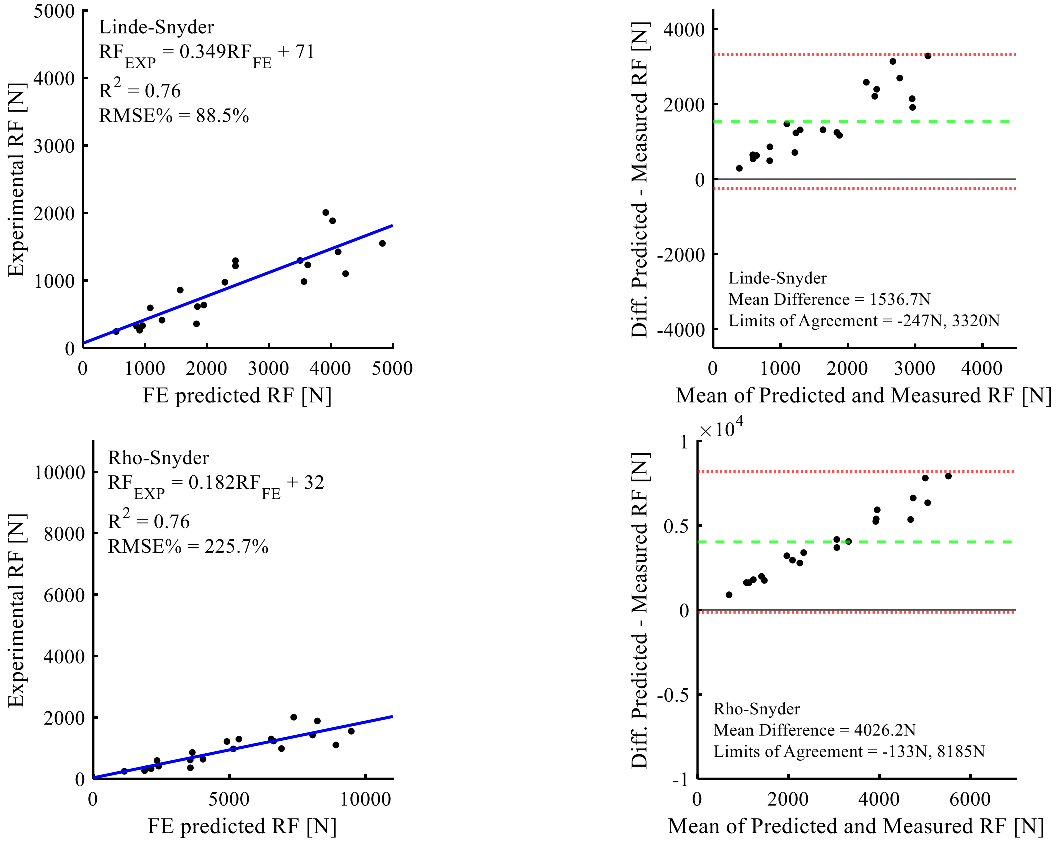

Figure A-2 Linear regression and Bland-Altman plots omitted from Chapter 5, for the various trabecular models combined with the cortical model of Snyder and Schneider. Blue lines are the least-squares fit regressions, red lines indicate LOA (+/- 1.96 SD) for Bland-Altman plots, and green lines indicate the mean difference between QCT-FE and DVC. Note the different scales for the trabecular relationship of Rho et al.